ENHANCED LUMINESCENCE FROM EUROPIUM DOPED YTTRIUM OXIDE THIN FILMS GROWN VIA PULSED LASER DEPOSITION

By

SEAN LIAM JONES

A DISSERTATION PRESENTED TO THE GRADUATE SCHOOL
OF THE UNIVERSITY OF FLORIDA IN PARTIAL FULFILLMENT
OF THE REQUIREMENTS FOR THE DEGREE OF
DOCTOR OF PHILOSOPHY

UNIVERSITY OF FLORIDA

1997

Copyright 1997

by

Sean L. Jones

To my Grandmother Ethell and Grandfather Russell Hughes, Uncle Eddie Jones, and best friend Edith Renee Hill who passed while I was on this part of life's journey, this volume is respectfully dedicated.

ACKNOWLEDGMENTS

I first give honor and praise to God for allowing me to see this day. Along with the Creator, my family and girlfriend are directly responsible for this achievement. I especially thank my mother. I thank her for her sacrifices, devotion, and little nudges to get me through the process. I would also like to thank Dr. Holloway for giving me the opportunity to contribute. He has been an untiring source of wisdom and inspiration. In that vain, I would also like to acknowledge Dr. Singh, who has served as a second advisor. I appreciate all of the individual time you have spent on this project and on my development. I would also like to thank the balance of my committee for their service: Dr. Hummel, Dr. Pearton, and Dr. Anderson.

I am particularly thankful for Dr. Jengyi Yu, the first graduate student I was paired with upon arrival to the University of Florida. He was my first mentor and colleague. For that, I will always be grateful to him. I would also like to recognize Dr. John M. Anderson, Dr. William Edmondson, and Dr. Paul Mason for their mentoring and friendship. Special recognition belongs to Dr. Hendrick Swartz, Dr. Mark Davidson and Xiao-Ming Zhang for their support. The three of them came into my life just as I was giving up hope and preparing to leave school to begin a new life. Their interest in me and my work kept me here far longer than I thought possible.

I would also like to thank Dr. Maggie Lambers for her assistance with SIMS data, Dr. Eric Lambers for his assistance with AES data, Richard Crockett for his help with SEM micrographs and EDS data, and Dr. Wayne O. Holland at Oak Ridge National Labs for his assistance in collecting RBS data. In that venue, I thank all those in Dr. Holloway's group and Dr. Singh's group for their assistance. I thank Ludie, Paula, Dorothy, Nigel, Wishey, Balu, Brent, Ananth, Karen, Mark, Steve, Jeff, TJ, Amondrea, Keith, and Michelle for their friendship over the years. Special thanks go to Ludie for keeping the office running smoothly and putting up with all of us.

Special acknowledgments go to the McKnight Doctoral family, members of the Black Graduate Student Organization, National Society of Black Engineers, Traveler's Rest Baptist Church, Mt. Moriah Baptist Church, and Mt. Carmel Baptist Church. I am also grateful to the Brothers of Nu Eta Lambda, Theta Sigma and Pi Alpha chapters of Alpha Phi Alpha Fraternity, Incorporated.

TABLE OF CONTENTS

ACKNOWLEDGMENTS iv

ABSTRACT viii

CHAPTERS

1. INTRODUCTION 1

2. LITERATURE REVIEW 8

  Field Emission Displays 8
  Yttrium Oxide:Eu^{+3} (Y_2O_3:Eu) 12
  Cathodoluminescence 16
  Efficiency of Thin Film Phosphors 19
  Elementary Scattering Theory 23
  Luminescent Thin Film Research 28
  Pulsed Laser Deposition (PLD) 32

3. EXPERIMENTAL PROCEDURE 54

  Substrate and Target Preparation 54
  Pulsed Laser Deposition(PLD) 55
  PLD Film Characterization 57
    X-Ray Diffraction(XRD) 57
    Scanning Electron Microscopy(SEM) 60
    Rutherford Backscattering Spectroscopy(RBS) 60
    Atomic Force Microscopy(AFM) 62
    Auger Electron Spectroscopy(AES) 65
    Photoluminescence(PL) 66
    Cathodoluminescence(CL) 67

4. RESULTS 76

  Photoluminescence(PL) 76

Cathodoluminescence(CL) 78
Thin Film Growth 80
Surface Roughening 82
Annealing 85

5. DISCUSSION 136

Enhanced Luminescence Through Scattering 136
CIE Coordinates and Reduced Luminescence 139
Thin Film Growth 141
Annealing 144

6. SUMMARY AND CONCLUSIONS 164

7. FUTURE WORK 168

APPENDICES

A CALCULATION FOR FRACTION OF LIGHT EMITTED 171
B ALLOWED (hkl) VALUES FOR X-RAY DIFFRACTION 172

REFERENCES 173

BIOGRAPHICAL SKETCH 182

Abstract of Dissertation Presented to the Graduate School
of the University of Florida in Partial Fulfillment of the
Requirements for the Degree of Doctor of Philosophy

ENHANCED LUMINESCENCE FROM EUROPIUM DOPED YTTRIUM OXIDE THIN FILMS GROWN VIA PULSED LASER DEPOSITION

By

Sean Liam Jones

December 1997

Chairman: Professor Paul H. Holloway
Major Department: Materials Science and Engineering

Yttrium oxide thin films doped with europium were grown on silicon, Corning 2947 glass, c-axis sapphire and quartz substrates. A pulsed laser ablation process was used to deposit films onto substrates heated from 250 °C to 800 °C and at oxygen pressures between 10^{-5} Torr and 600 mTorr. The deposited films were characterized using x-ray diffraction, secondary electron microscopy, Auger electron spectroscopy, atomic force microscopy, secondary ion mass spectroscopy, photoluminescence and cathodoluminescence.

Crystalline as-deposited films were achieved at substrate temperatures as low as 250 °C. Films grown in high vacuum were strongly (111) textured, but became more random polycrystalline as the temperature was increased to 800 °C and/or growth pressure was increased to 600 mTorr. The root mean

square roughness increased significantly as oxygen pressure increased. Films grown at 10^{-5} Torr had RMS roughness values of 2-3 nm, but the roughness increased to 71 nm for growth at 600 mTorr. Above 200-300 mTorr oxygen, the film morphology changed from a smooth to a particulate surface. These particles were 100 ± 15 nm at the transition pressure and decreased to 80 ± 15 nm at 600 mTorr. During annealing, the grain size remained well below 200 nm, even after 1400 °C for 1 hour.

Photoluminescence and cathodoluminescence intensities increased as a function of increasing growth temperature and pressure. PL was done using a UV lamp with a wavelength of 254 nm as the excitation source. A PR 650 camera with an internal calibrated intensity standard was used as the detector. The PL intensity increased from 0.093 fL for 1 μm thick films grown at 10^{-5} Torr to 0.81 fL for films grown at 600 mTorr. The powder gave 11 fL. The PL response from the film increased to 4 fL (36% that of the powder) for a the thickness of 9 μm.

Cathodoluminescence was done using a Kimball Physics EFG7 electron gun and an Ocean Optics S2000 fiber optic as the detector. Films were not cathodoluminescent until growth and annealing at 800 °C or higher. The best brightnesses were observed at temperatures > 1170 °C. This temperature corresponds to 0.54 of the melting temperature for yttria. At 2 kV and 1 μA/cm^2, 3 μm thick films grown at 100 mTorr (RMS of 3 nm) had CL efficiencies of 0.85 lm/W, at 600 mTorr (RMS of 71 nm) had efficiencies of 2.63 lm/W, while the powder had an efficiency of 9.5 lm/W. The CL efficiency for a 9 μm thick rough film was 3.3 lm/W at 2 kV and 1 μA/cm^2.

The CIE color chromaticity coordinates (x, y) of the films were different from the powder {(x, y) of (0.62,0.35) for film instead of (0.644, 0.35) for powders}, indicating that the concentration of active europium was lower in the films, by as much as one mole percent. This contributed significantly to lower CL efficiencies for the films. This was confirmed with RBS.

Improvements in luminescence with an increase in surface roughness were attributed to forward light scattering caused by the rough surface. The increase in light scattered at the surface was presumed to reduce the percentage of light internally reflected within the film. The appropriate scattering model was anomalous diffraction. Although the 3 μm thick rough film was only 27.7% as efficient as the powder, anomalous diffraction theory predicts that increasing the roughness to 200 nm would yield an efficiency of 12.7 lm/W (134% that of powder).

CHAPTER 1

INTRODUCTION

Much of the interest in field emission displays (FEDs) is due to the large number of applications that would benefit from their realization. These flat panel displays (FPD) are thinner, lighter, and consume less power than conventional displays, such as the cathode-ray tube (CRT). Since the FED will operate between 100 V and 5 kV, be significantly thinner and lighter, it is the prime choice for notebook computers and 'thin TVs' over CRTs. See figure 1-1. Field emission displays also provide significant improvements over the more common of the FPD technologies, liquid crystal displays (LCDs).[Cas92] Table 1-1 shows a comparison of LCD versus FED technology.[Hol96] The improved brightness, power efficiency, viewing angle and temperture range make an FED the choice for laptop computers. For applications such as military and medical, the reduced weight, lower power consumption, and wider operating temperature range give FEDs a further advantage over LCDs.

Economic incentives have also fueled increased research interest into developing this technology. It is estimated that the FPD industry will be a $20 billion market by the year 2000.[DeJ97] Table 1-2 illustrates the market share for the various display technologies, where the price per display is given in the parenthesis. As noted, the anticipated unit price for an FED is considerably lower than that for LCDs or electroluminescent displays (ELD), the main competing technologies.[DeJ97] The FED industry could be a half billion dollar business by the year 2003 by filling niche markets alone.

The research presented in this thesis is primarily for advancing FED technology. Current FED phosphor powder research is concerned with increasing the efficiency and lifetime while reducing particle size. Reducing the particle size allows for smaller pixels, yielding higher resolution. As the optimized CRT phosphor powder particles are reduced in size, however, the efficiency decreases significantly.

An alternative phosphor configuration, thin films, was studied in this research. By overcoming some of the fundamental limitations of thin films, several advantages would be realized. Table 1-3 lists the advantages and disadvantages of powders versus thin films.[Fel57a] The intent of this reserach was to show that modifing the surface could increase the efficiency of thin film phosphors.

In this dissertation, the literature is reviewed in chapter 2 to provide a background for this work. A brief overview of FED technology, an outline as to why thin films are less efficient, a review of applicable scattering theory, and a review of the pulsed laser ablation technique are presented. Past phosphor thin film research is reviewed to place the gains achieved from this study into proper perspective. The experimental procedures used to deposit the Y_2O_3:Eu thin films are described in chapter 3, along with a variety of techniques for thin film characterization. A brief outline of each technique is given with emphasis placed on photoluminescence and cathodoluminescence. Results are presented in chapter 4. A discussion of results follows in chapter 5 with an emphasis on crystal quality and luminescence. Conclusions from this work are presented in chapter 6, and future studies in chapter 7.

Table 1-1 Comparison of FED and LCD Technologies

CHARACTERISTIC	FED (target)	TFT-LCD
Thickness	6-10 mm	23 mm
Weight	<0.2 kg	0.33 kg
Contrast ratio	>100:1	100:1
Viewing angle	160° V, 160° H	±60° V, ±90° H
Max. brightness	>200 cd/m^2	60 cd/m^2
Power @ 60 cd/m^2	<1 W	4 W
Max. Temperature	-50 to + 80 °C	0 to 50 °C

[Hol96]

Table 1-2 Market Share information for Flat Panel Displays

Display	1997	1998	1999	2000	2001	2002	2003
LCD-TFT	$8407 ($316)[a]	$9917 ($306)	$11743 ($298)	$14317 ($296)	$16227 ($282)	$17905 ($264)	$19165 ($242)
EL	$115 ($442)	$124 ($449)	$135 ($464)	$152 ($483)	$168 ($494)	$187 ($507)	$207 ($517)
Plasma	$325 ($1014)	$416 ($1143)	$665 ($1387)	$964 ($1530)	$1466 ($1640)	$2085 ($1641)	$2357 ($1548)
FED	$1 ($169)	$5 ($144)	$35 ($165)	$94 ($173)	$219 ($167)	$333 ($143)	$444 ($132)
LED[b]	$542 ($3)	$552 ($3)	$567 ($3)	$572 ($3)	$586 ($3)	$601 ($3)	$617 ($3)
Vacuum[b]	$752 ($5)	$769 ($5)	$791 ($5)	$806 ($5)	$815 ($5)	$821 ($5)	$826 ($5)

[a] Estimated sales revenue in millions of dollars. (Unit selling price in dollars.)

[b] These displays are alpha-numeric displays which are extremely small.

[DeJ97]

Table 1-3 Advantages and Disadvantages of Thin Film versus Powder Phosphor

	THIN FILM PHOSPHOR	PHOSPHOR POWDER
Efficiency	poor	excellent
Resolution	$<< 1\mu m$	$5\ \mu m$ to $10\ \mu m$
Screen Contrast	excellent	good
Lifetime(at high $\mu A/cm^2$)	good	poor
Mechanical Stability	excellent	good
Thermal Stability	excellent	good

[Fel57a]

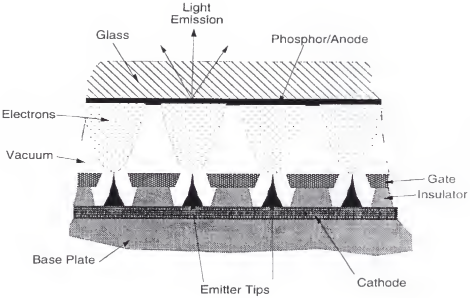

Figure 1-1. Spindt cathode type field emission display (FED). The Spindt type is the most common FED structure.

CHAPTER 2

LITERATURE REVIEW

Field Emission Displays

Flat panel displays (FPDs) may be divided into two classes, emissive and non-emissive.[Tan85] Non-emissive displays do not emit or radiate light, but act as light valves for back lighting sources. In emissive displays, however, luminescent materials are excited by an energy source and subsequently radiate light. These luminescent materials are called phosphors. Field emission displays operate on the same principles as coventional cathode ray tubes (CRTs).

In a CRT, a triode e-gun cathode is used to generate and accelerate electrons toward a phosphor screen.[Cas92] The cathode beam is scanned across and rastered down the display illuminating one red, green, or blue (RGB) phosphor pixel at a time. Scanning and rastering are accomplished by deflecting the beam with magnetic coils. The scanning and rastering requirement primarily accounts for the depth and bulk of CRTs.

In an FED, scanning and rastering are not used. Instead, an array of field emission tips generate the electrons. Refer to figure 1-1. Upon applying a very low voltage across the gate, electrons are emitted from the cone shaped tips and are accelerated toward the phosphor screen. When the electrons strike the phosphor screen, cathodoluminescence occurs. Cathodoluminescence (CL) is the emission of light upon electron radiation.

These FED tips can be turned on one row of pixels at a time, eliminating the need to deflect the electron beam. This eliminates the path needed for electron deflection, therefore, the FED is a flat panel display technology. Different geometries of field emission displays are shown in figures 1-1 and 2-1, where the tips in figure 1-1 are referred to as a Spindt cathode, the more common type. The second type is an edge emitter which offers another configuration where the whole device is on one substrate. For both, the spacing between the base and the face plate is on the order of a 1 to 3 millimeters. The whole display, including packaging, is thinner than 5 centimeters.

Charles A. Spindt developed field emitter tip technology in 1973 at SRI International using VLSI processing.[Mat86] The emitter tips are metals such as W and Mo, or semiconductors such as Si and diamond. When a voltage is applied between the tip and the gate, Fowler-Nordheim tunneling [Hud92] occurs and electrons are accelerated toward an anode. These tips emit electrons above 20 V compared to etched wire emitters which require between

1 to 3 kV.[Adl91, Spi76] Low voltage operation yields stable, continuous emission with long tip life. Field emission current density, J [A/cm^2], due to Fowler-Nordheim tunneling is described by Brodie and Spindt:

$$J = 1.54 \; x \; 10^{-6} \frac{E^2}{\Phi t^2(y)} \exp(-6.87 \; x \; 10^7 \frac{\Phi^{3/2}}{E} \; v(y))$$

where E is the applied electric field [V/cm], Φ is the work function [eV], $t^2(y)$ is approximately 1.1, and y is the Schottky image charge lowering contribution to the work function.[Bro92] The variable $t^2(y)$ is explained in detail elsewhere. [Adl91,Cut93]. The variables v(y) and y are equal to

$$v(y) = 0.95 - y^2$$

and

$$y = 3.79 \; x \; 10^{-4} \; \frac{E^{1/2}}{\Phi}.$$

Figure 2-2 shows J as a function of electric field for varying work functions. Even with low voltages acting over closely spaced electrodes, current densities greater than 10^6 A/cm^2 are possible.

Semiconductor field emission tips are degenerately doped ($\approx 10^{19}$ cm^{-3}) so that the Fermi level is just above the bottom of the conduction band. In such a case, the work function term in the Fowler-Nordheim equation is replaced with the semiconductor's electron affinity, χ.[Bro92] The electron affinity is the energy needed to raise an electron from the bottom of the conduction band to the vacuum level.

Utsumi [Uts91] showed that the tip shape is also critical in determining the turn-on voltage and field emission current density. He concluded that round whiskers were closest to ideal emitters. Cutler [Cut93] reported that higher current densities were possible by reducing the tip radius, as seen in figure 2-3.

The other half of the display is the phosphor screen. Phosphor powder can be applied to glass plates using electrophoretic, dusting, or slurry methods.[Has90] The slurry method is the most common where phosphor powder is mixed with photosensitive chemicals and deposited using photolithography techniques. For operating voltages greater than 2 kV, the screen is back coated with a thin layer of aluminum as a reflector and charge dissipater.[Lev68] At operating voltages below 2 kV, the electron penetration depth is so small that the screens are left un-coated.[Bec96] In this study, the starting phosphor powder was yttrium oxide powder doped with four and a half weight percent of europium obtained from Osram Sylvania.

Yttrium Oxide: Eu^{+3} (Y_2O_3:Eu)

Yttrium oxide (Y_2O_3), commonly referred to as yttrium sesquioxide or yttria, is a highly refractory oxide with a melting point of 2410 °C. At room temperature yttria is a body centered cubic with the bixbyite or cubic-C structure with a lattice parameter of 10.6 Å.[Wyc64] There is an allotropic phase transformation to hexagonal at 2367 °C.[Tro91] Yttria has very good chemical stability, high resistivity and a high dielectric breakdown strength. It has a measured room temperature bandgap of 5.3-5.5 eV [Jol90] and a bandgap of 5.8 eV at 10 °K.[Tom86]

Yttria has a theoretical density of 5.033 g/cm^3. There are 16 molecules of 80 atoms in its unit cell. The cation occupies two different crystallographic sites, S_6 and C_2, as seen in figure 2-4. There is a full layer of C_2 sites with a layer of alternating S_6 and C_2 sites, resulting in 75% of the yttriums in C_2 symmetry and 25% in S_6 symmetry. In S_6 symmetry, the yttrium is in contact with body diagonal vacancies, but in contact with face diagonal vacancies in C_2 symmetry. In both symmetries, the cation is surrounded by 6 oxygens.[Mae92] These sites are, therefore, chemically equivalent but crystallographically different. S_6 symmetry is also denoted in the literature as C_{3i} symmetry.

Yttria is a perfect host for the trivalent rare earth europium to make highly efficient lamp and cathodoluminescent phosphors. Europium belongs to the Lanthanide series which is characterized by an unfilled 4f electron shell surrounded by filled 6s and 5p shells. Europium can have either a Eu^{+2} or a Eu^{+3} valence where the electron configurations are (Kr core) $4d^{10}4f^{6}5s^{2}5p^{6}5d^{1}$ and (Kr core) $4d^{10}4f^{6}5s^{2}5p^{6}5d^{0}$, respectively. See figure 2-5. Note that due to the electron shell filling rules, the 4f level is partially filled until the 5d shell has been completely filled. In yttria, Eu substitutes for the Y in both the S_6 and C_2 sites.

For the Lanthanide series rare earths, the deep lying 4f electrons are shielded from the effects of the host lattice by the 6s and 5p shells. This gives rise to a number of discrete energy levels that, due to the shielding, resemble the energy level diagram of a free ion.[Bla94] Since the excitation and emission occur within the discrete levels of the 4f shell, a characteristic sharp line emission ^5D_J to ^7F_J results. See figures 2-6 and 2-7.

The allowed transitions (^5D_J to ^7F_J) from the activator, Eu^{+3}, are a function of the selection rules.[Hen89] Three types of transitions are possible: electric-dipole (ED) transitions, magnetic dipole (MD), and electric quadrapole (EQ) transitions. The strength of these transitions decreases from ED to MD to EQ as the ratio $1:10^{-5}:10^{-6}$. The weaker MD and EQ transitions are usually allowed, so we are concerned with the selection rules governing ED transitions. Laporte's rule states that electric dipole transitions within the 4f level are forbidden due to unchanged parity. Parity refers to the state of the orbital angular momentum quantum number, l, which can be even or odd.

Since the 4f to 4f transitions occur within the same quantum number, the parity does not change and are, therefore, not allowed.

Laporte's parity rule, however, can be lifted if there is mixing of parity from the lattice.[Bla79] When the luminescent center is in a crystal site that does not have inversion symmetry, there will be a mixing of parities and LaPorte's rule is lifted. Lifting of the parity rule can result in a transition. This is called a forced transition. If the site retains inversion symmetry, Laporte's rule is upheld and no luminescence is observed from the ion. In yttria, europium occupies both C_2 and S_6 sites. The S_6 site has inversion symmetry but the C_2 site does not. This yields both an ED and MD transition where the MD originates from the S_6 and C_2 sites and a forced ED transition originates only from C_2 sites. The primary emission peak at 611 nm for Y_2O_3:Eu^{+3} originates from forced ED transitions from Eu in C_2 cation sites because of inversion symmetry.[For69]

The specific levels from which these transitions occur are also controlled by the selection rules. The Jodd-Ofelt's theory adds that the allowed ED (^5D_J to ^7F_J) transitions must adhere to the following:

1) $\Delta J \leq 6$,

and for an f shell filled with an even number of electrons:

2) when $J = 0$ then $J' = 0$ is forbidden,
3) if $J = 0$ then odd J' values are weak (MD),and
4) if $J = 0$ then $J' = 2,4,6$ are strong.[Hen89]

In this case, europium has 6 electrons in its 4f shell. According to the Jodd-Ofelt theory, a strong $^5D_0$-$^7F_2$ ED transition is expected to be accompanied by weaker $^5D_0$-$^7F_1$ MD transitions. This explains the characteristic sharp line emission peak at 611 nm ($^5D_0$-$^7F_2$) from Y_2O_3:Eu^{+3} seen in figure 2-7. Blasse [Bla79] concludes that orange-red ($^5D_0$-$^7F_1$) emission results from europium ions that occupy centers of inversion symmetry, and Eu^{+3} in sites that lack symmetry emit in the red ($^5D_0$-$^7F_2$) and infra-red ($^5D_0$-$^7F_4$).

The site symmetry and site coordination will determine the number of primary peaks seen for these transitions. For J values equal to 0, splitting of levels is not allowed. For J> 0, triple degeneracy is possible and splitting can occur. The field symmetry also determines the amount of allowed splitting. Cubic symmetry does not cause splitting but tetragonal and trigonal fields cause splitting into 2 levels. Lower symmetry sites cause splitting into three levels yielding three peaks.[Bla79] Since the emission for Y_2O_3:Eu originates from a $^5D_{J=0}$ level, only one peak is allowed. And since the Eu predominantly sits in a cubic symmetry site, the $^7F_2$ level is not degenerate and no splitting occurs. Thus only one primary $^5D_0$-$^7F_2$ peak is seen.

The selection rules also help determine the speed of these transitions. The Eu^{+3} has an excited state lifetime of approximately 10^{-3} seconds which is ≈ 10^5 times longer than the lifetime for allowed electric dipole transitions. This difference in lifetimes illustrates the degree to which these forced ED (4f to 4f) transitions are forbidden.[Bla79] Details of this transition via cathodoluminescence are given below.

Cathodoluminescence

The term phosphor is reserved for materials that display phosphorescence and/or fluorescence when excited with an energy source. Phosphorescence is the non-thermal radiation that persists after the excitation event has ceased. Fluorescence refers to non-thermal radiation given off while the incident energy impinges the sample. Radiation that does not terminate within 10 nanoseconds of energy excitation is classified as phosphorescence. The incident energy can be in the form of X-rays, UV photons, energetic ions, electrons, or result from mechanical disruption.[Mar88, Lev68] The types of luminescence are chemiluminescence which is initiated by a chemical reaction, photoluminescence obtained from photons, roentgenoluminescence from X-rays, ion luminescence from energetic ions, electroluminescence induced by an electric field or current, incandescence resulting from high temperatures, and cathodoluminescence resulting from electrons.[Lev68] Cathodoluminescence contains components from both phosphorescence and fluorescence. Figure 2-8 and 2-9 depict qualitatively the interactions that occur after an electron impinges on a surface. As seen in figure 2-8, there are a number of physical processes that result from the primary beam interaction with the solid. The depth that an energetic electron will penetrate into a solid is dependent on the voltage. Figure 2-9 shows the excitation volume shape and depth as a function of voltage. The number of luminescent centers excited is controlled by the depth of the incident electrons and follows Terril's formula for penetration depth:

$$x = 2.5 \; x \; 10^{-12}\rho^{-1}V_o^2 \quad [cm]$$

where ρ is the material's density and V_o is the voltage.[Fel60] This equation is valid for 1 to 10 kV. Figure 2-10 shows that for 10 kV electrons incident on yttria the range is 500 nm, but is reduced to 125 nm for 5 kV electrons. The observed luminescent area and intensity will be a function of the beam energy, electron-hole pair generation and diffusion, subsequent emission processes, competing absorption processes, and in the case of thin films, the amount of internal reflection of photons.[Gol66]

The process by which the electrons travel to the rare earth activators to excite them is different from the classical donor and acceptor model. Process 7 of figure 2-11 depicts the excitation and deexcitation from an impurity with incomplete inner shells like rare earths and transition metals.[Yac92] Processes 4,5, and 6 are transitions expected from classical donors and acceptors impurities that establish localized states in the band gap.

The mechanism by which the electron and holes travel to the activator is explained by Ozawa.[Oza71] Cathodoluminescence in phosphors is initiated by

1 of 3 mechanisms, (i) absorption from energy transferred from the host to the activator, (ii) direct absorption by the activator ion from the incident energy, and (iii) indirect excitation by the absorption of energy by recombination of mobile electrons and holes, where processes (ii) and (iii) dominate. By using concentration dependence (CD) curves (figure 2-12), the method of transfer may be revealed. Phosphors whose CD curves contain only one inflection for concentration quenching are excited directly by the electron beam (figure 2-12b, Y_2O_3:Pr). CD curves that have two inflection points (figure 2-12a and b) Y_2O_2S:Pr) are from phosphors that are excited indirectly by mobile electron-hole pairs (EHs). In the case of indirectly excited phosphors, the first inflection in the CD curve corresponds to the luminescence from electron-hole pairs that have diffused beyond the primary beam range. Note that all of these phosphors display direct excitation CD curves under photoluminescence.[Oza90]

The process of cathodoluminesce by indirect excitation through recombination of mobile carriers is as follows for Y_2O_3:Eu^{3+}.[Oza68, Die68] When the cathode ray impinges the host lattice, electron-hole pairs are created. The electrons and holes are free to migrate within the crystal. The migration distance is given by

$$L = dC^{-1}$$

where L is the migration distance or the distance an electron or hole must travel from the host ion to an activator, d is the distance between cations and

C is the average number of activator ions to cations.[Oza90] The model assumes that the lattice ions do not act as recombination sites for the EHs and that recombination only occurs at the activator ion. The incident electron coverts the yttrium, Y^{3+}, to Y^{2+}. The divalent yttrium quickly releases the electron to the next yttrium, converting back to Y^{3+}. The model also assumes that conversion of Y^{2+} to Y^{1+} is not possible. The electron migrates along the Y^{3+}s until it reaches an activator, Eu^{3+} in this case. The europium, having trapped the electron, is converted to Eu^{2+}, which results in a local field that is negatively charged. The holes, which are transported on the O^{2-} converting them to O^{1-}, are attracted to this negative charge region. Once the hole is captured by the Eu^{2+}, the europium goes into the excited Eu^{3+*} state. It relaxes and returns to the ground state (Eu^{3+}) emitting a photon with a characteristic wavelength. This process can be repeated continuously, limited only by the capture and decay time of the Eu^{3+*} state.

Efficiency of Thin Film Phosphors

Before discussing previous research done on thin film phosphors, a discussion as to why thin film brightness may be lower than powders is in order. It has been generally accepted that thin films will always be less efficient than powders, because it is estimated that 80 to 90 % of the light generated within the film is lost in frustrated internal reflections.

The phosphor quantum efficiency, η_{eff}, under electron beam bombardment may be expressed according to Robertson and van Tol:

$$\eta_{eff} = \eta_t \eta_a \eta_{esc} \frac{(1-r_b)h\nu_{em}}{\beta E_g}$$

where r_b is the fraction of electrons backscattered, $h\nu_{em}$ is the average energy of the emitted photons, and η_t, η_a, and η_{esc} correspond to the efficiency of transferring the generated electron-hole pairs to the luminescent center, the efficiency of radiative recombination at the luminescent center, and the fraction of light escaping the sample, respectively.[Rob80] The minimum energy needed to create an electron-hole pair is represented by the constant, β, times the band gap,E_g. The constant β varies from 2 to 8 [Has90, Bec96], but is usually set equal to 2.8 [Ait93]. For phosphor powders, it is assumed that all of the luminescent centers are active, in the proper crystallographic sites, and that once the light is generated within the powder, there are enough reflections that all of the light escapes with minimum absorption. Thus η_a and η_{esc} are equal to one.[Bec96]

For thin film phosphors, however, these assumptions may not be valid. For poor crystalline quality films, the transfer of electron-hole pairs to luminescent centers and the probability of radiative recombination at the luminescent center will be lower than unity. The overall efficiency is further reduced by a low value of η_{esc} due to internal reflections (figure 2-13). For thin films with good crystallinity and optimized activator, internal reflection and absorption is a major loss factor as explained by the following.

Light impinging on an interface between two different media with different optical indices, will be reflected and refracted. Specifically, when light traveling at some angle θ_1 reaches the interface, the wave is refracted according to Snell's law

$$n_1 \sin\theta_1 = n_2 \sin\theta_2$$

where n_1 and n_2 are the indexes of refraction for each media and the θ_1 is the angle of the incidence light and θ_2 is the angle at which the light refracts. When medium 1 is more dense than medium 2 ($n_1 > n_2$), an angle exist where above its value, incident light is not refracted but is totally reflected back into the film. This angle is called the critical angle for total internal reflection, θ_c, and is equal to

$$\theta_c = \sin^{-1}\left(\frac{n_{air}}{n_{phosphor}}\right)$$

where n_{air} and $n_{phosphor}$ are the index of refraction for air and the film, respectively. See figure 2-13, where ray c is incident at θ_c and ray d is incident at an angle $> \theta_c$. Air has an n value of 1. Yttria has an index of refraction (at 611 nm) value of 1.93, yielding a θ_c of 31°. Figure 2-14 shows the change in the critical angle as $(1/n_{phosphor})$ is varied.

From the critical angle, a cone of emission forms where the volume of the cone is a function of the critical angle. The fraction of light, f, that will escape the thin film through this cone is approximated geometrically by

$$f = \frac{(1-\cos\theta_c)}{2} = \frac{1}{4n_{phosphor}^2}.$$

as is detailed in Appendix A.[Car66] If emission is measured from only one surface and if light propagating in the other direction is not reflected but is lost, only 7% of the light would be transmitted out of yttria thin films. The light impinging within this projection cone, is further subjected to the standard rules for reflection and transmission across the interface. The percentage of the light within the cone that will be transmitted, T, for a dielectric thin film is given by

$$T = \frac{4n_{phosphor}}{(n_{phosphor}+1)^2}$$

and for yttria, approximately 10% will be reflected and not transmitted, resulting in only 6.3% of the light leaving the thin film. Even if backside reflections were included, the maximum output would be 13%.

This is analogous to waveguiding in fiber optic systems, where the cladding layer has an index of refraction which keeps the light trapped within the fiber. In thin film phosphors, this waveguiding effect is termed "light piping". It can be seen from this discussion that perceived brightness can be severely reduced in thin film phosphors, leading to lower efficiencies.

Elementary Scattering Theory

It will be shown in the following chapters that roughening the surface of a dielectric thin film phosphor increases the photoluminescence (PL) and cathodoluminescence (CL) brightness. Since this increase was attributed to scattering at the film/air interface, an outline of scattering and how it pertains to particles and films is presented. Although there is an abundance of scattering theories, ranging from general to case specific solutions, the discussion below is limited to solutions for nonconducting, non-absorbing, relatively small particles with refractive indices close to 1. A brief overview of applicable scattering theory is presented below.

It is generally accepted that scattering refers to the movement of a wave due to the presence of an obstacle of a given size, form and composition. [Van81] More specifically, the term is most applicable when the 'obstacle' has a size smaller than the incident wavelength, λ. The 'movement' due to an obstacle having a size much greater than λ is referred to as diffraction, reflection, or refraction.[Van81, Jen76]

For spherical particles, scattering occurs when the radius, a, is much smaller than the wavelength, but geometric optics apply when $a > \lambda$. Thus, the first important parameter for scattering due to spherical particles is the particle size. The size parameters that describe this scattering are x, and ρ, given by the following equations:

$$x = \frac{2\pi a}{\lambda}$$

and

$$\rho = 2x|n-1| \ ,$$

where a and n are the radius and the index of refraction of the sphere, respectively.[Van81] For the case of nonconducting, non-absorbing, relatively small spheres (small x and ρ) with refractive indices close to 1, the following scattering conditions apply; Rayleigh scattering, Rayleigh-Gans scattering, intermediate scattering, anomalous diffraction or the limiting case of geometric optics where $a>\lambda$. The x and ρ requirements to meet each condition are presented below with their effect on scattering.

The most well known of scattering theories is Rayleigh scattering, developed by Lord Rayleigh in 1881.[Str64] Rayleigh scattering occurs when, (a) the external field can be considered as a homogenous field across the particle, mathematically expressed as

$$a \ll \frac{\lambda}{2\pi} \ ; \ x \ll 1,$$

and (b) the particle size and index of refraction are smaller than the wavelength inside the particle, λ/n, which is mathematically expressed as

$$|n|a \ll \frac{\lambda}{2\pi} \quad ; \quad nx \ll 1 \ .$$

A particle size of less than $\lambda/20$ can be used as a guide.[Van81] Thus, when the x and n*x values are much less than 1, Rayleigh scattering yields a scattering efficiency, Q_{sca}, equal to:

$$Q_{sca} = \frac{8}{3} x^4 \left| \frac{m^2-1}{m^2+1} \right|^2 ,$$

showing the well known $(a/\lambda)^4$ dependence, since x is equal to $(2\pi a/\lambda)$.[Str64] This is the Rayleigh scattering formula for nonconducting, non-absorbing spheres as opposed to the more common formula expressed for $n \rightarrow 1$. The term Q_{sca} is the cross-section for scattering, C_{sca}, normalized by the particle's area projected perpendicular to the incident beam.[Boh95]

As the sphere size increases, the scattering condition moves from Rayleigh to Rayleigh-Gans scattering [Van81], where the two main assumptions are that (a) the index of refraction is close to 1 and (b) the allowable phase shift is small such that

$$a < \frac{\lambda}{4\pi|n-1|} \ .$$

The difference between Rayleigh and Rayleigh-Gans scattering is that a larger phase shift is allowed. The scattering efficiency, Q_{sca}, is expressed as an integral that is bound by two limiting cases of x << 1 and when x >>1, where the efficiency is expressed as

$$Q_{sca} = |n-1|^2 \psi(x).$$

The function $\psi(x)$ is an integral equal to

$$\psi(x) = \frac{5}{2} + 2x^2 - \frac{sin4x}{4x} - \frac{7}{16x^2}(1-cos4x) + (\frac{1}{2x2} - 2)[0.577 + log4x - Ci(4x)]$$

where Ci(4x) is a cosine integral bound by x and ∞. When x <<1, the Rayleigh scattering condition is obtained. As x becomes large and x(n-1) remains small, the scattering changes from a $(a/\lambda)^4$ to a $(a/\lambda)^2$ dependence and is expressed as

$$Q_{sca} = 2(n-1)^2 x^2 = 0.5\rho^2 .$$

This is the beginning of the intermediate scattering condition. Rayleigh-Gans scattering can be thought of as being bound by the two extremes, Rayleigh scattering and intermediate scattering. As seen by the formula, intermediate scattering has a $(a/\lambda)^2$ dependence.

As x or n are increased further, the scattering condition changes again to anomalous diffraction where the scattering efficiency is expressed in terms of a sine integral:

$$Q_{sca} = 2 - \frac{4}{\rho}\sin\rho + \frac{4}{\rho^2}(1-\cos\rho) \ .$$

Here, the assumptions are that x and ρ are large, where large is any value close to or greater than 1.[Van81] Anomalous diffraction, just as Rayleigh scattering, can also be used with large n values. As radius, a, becomes larger than the wavelength of light, anomalous diffraction moves into geometric optics, where the classical diffraction, reflection, and refraction rules are appropriate.[Jen76]

In summary, scattering theory can be applied to particles, but the particle size, wavelength of incident light and refractive index determine the type of scattering which occurs. For extremely small particles, Rayleigh scattering dominates, having a $(a/\lambda)^4$ dependence. As the particle size and index are increased, Rayleigh-Gans scattering applies, having a dependence ranging from $(a/\lambda)^4$ at low x to $(a/\lambda)^2$ at larger x. Once the x and x(n-1) values reach unity, or larger, scattering is described by anomalous diffraction with an integral that leads to between $(a/\lambda)^2$ and a $(a/\lambda)^3$ dependence for small and large radius, respectively. For particle radii greater than the wavelength of light, geometric optics, such as ray tracing, should be used.

Luminescent Thin Film Research

Williams [Wil47] was the first to publish data on the deposition of thin films for cathodoluminescence phosphors. It was quickly realized that thin film phosphors would provide advantages over phosphor powders, namely that screens would be transparent and not opaque or white, improved resolution would be easily obtained, the thickness could be optimized versus operating voltages, and the thermal and electrical conductivities could be higher for continuous thin films. Refer to table 1-3. Recently, additional research has been reported on cathodoluminescent thin films whose efficiencies are shown in table 2-1.

The majority of studies of thin film luminescence have focused on electroluminescence (EL) and photoluminescence (PL) in thin films. Cathodoluminescence data have predominantly been collected from powders, due to the severe reduction of luminescence brightness observed with thin films versus powders.[Gol66] Much of the early thin film research worked on exploiting the advantages of thin film structures, such as fabricating penetron devices.[Fel57a] Penetrons are layered phosphor films that change emission color as a function of beam voltage due to change in penetration depth. (See figures 2-8 & 2-9.)

Current research has focused on the growth of high quality thin films and the quantification of thin film brightness. A variety of growth techniques have been employed, including evaporation, spray pyrolysis, sputtering, metal organic chemical vapor deposition and more recently pulsed laser deposition. Williams [Wil47] employed an evaporation technique to deposit Mn doped zinc fluoride phosphors. The thin films were grown at 100 °C and were luminescent as-deposited. However, these films degraded and decomposed readily under electron beam bombardment. Studer et al. produced ZnS:Mn [Stu51,Cus52] and ZnS:As,P [Stu55] using a chemical vapor deposition technique. They achieved white brightnesses of 20% that of the powder with the ZnS:As,P phosphor thin films. The films displayed an efficiency of 1.08 lm/W at 10 kV and 1 mA/cm^2. With the use of an integrating sphere, they also showed that the lower brightness could not be attributed to internal reflections alone, but lower crystallinity or the presence of defects reduced the efficiency. They subsequently showed that thin film phosphors exhibited high spatial resolution due to less light scattering.[Stu55,Stu56] Feldman et al. [Fel57b] deposited several phosphors via vacuum evaporation followed by high temperature vacuum anneals. They found low brightnesses for transparent ZnS:Mn films and a 2.5x improvement using a frosted substrate. Their high temperature, long time anneals turned the transparent films ‘foggy’ and opaque. These ‘fogged’ films were 90% the brightness of the powder. They deduced that the films were rough since they displayed the characteristic opaque color resulting from severe diffuse reflectance. They also showed that oxide phosphors like $(Zn_2PO_4)_3$, $CaWO_4$:W, and Zn_2SiO_4:Mn could be formed using vacuum evaporation. Koller et al [Kol60] evaporated ZnS:Mn in a H_2S and HCl background gas. This helped to maintain stoichiometry and to incorporate Cl into the film. They reported that while their films were crystalline as-deposited at 100 °C, they did not luminescence until heat treated at 650 °C. They also produced Zn_2SiO_4:Mn thin films by evaporating ZnF_2:Mn onto heated quartz (550 - 650 °C) substrates. Bateman [Bat60] also evaporated ZnS:Mn thin films and a MgF_2:Zn,Mn phosphor thin film. The MgF_2 phosphor performed as well as the ZnS:Mn thin film.

Kirk et al. [Kir61] used spray pyrolysis to react ZnCl with a heated silica substrate to make $ZnSi_2O_4$ doped with Mn and Ti thin films. They achieved thin film efficiencies of 0.24 lm/W as-deposited and 0.32 lm/W for films annealed at 1250 °C for 1 hr. Their beam conditions were 7.5 kV and 10 mA/cm^2. Spray pyrolysis was later used by Falcony [Fal92] to deposit ZnS:Mn films from which PL data were reported. Luminescence was achieved with substrate temperatures as low as 360 °C. With PL, they showed the reduction of a self-activated defects as the growth temperature was increased.

Hansen et al. [Han65] were the first to use electron beam evaporation to deposit phosphor thin films. Yttrium oxide doped with various rare earths was deposited onto heated molybdenum strips. They achieved 2.7% of the brightness of the standard powder for europium doped films, but 41% of the powder brightness for Tb doped. No explanation for the differences was given.

Dalacu et al [Dal92] later used electron beam evaporation to deposit $MgAl_2O_4$:Mn phosphor thin films. No brightness data were given.

Sputtering has also been employed to deposit cathodoluminescent phosphor thin films. Maple et al [Map73] deposited La_2O_2S doped with Eu^{+3} (red) and Tb^{+3} (green) and obtained the highest reported efficiencies of 7.37 lm/W at 1 W/cm^2 after a 1000 °C anneal in an H_2-SO_2 atmosphere. They also showed that beveled edges on 20 μm x 20 μm segments improved the efficiency by a factor of 3. Sella et al [Sel82] reported the deposition of amorphous Y_2O_2S and La_2O_2S thin films doped with Eu^{+3} and Tb^{+3}. The films were annealed to 600 to 850 °C to get good luminescence. Like Feldman, they reported an increase in brightness of 4x by using ground substrates over smooth ones. They also employed laser annealing via a pulsed CO_2 laser that showed a 3x improvement over furnace annealing. Bondar [Bon95] grew Y_2O_3:Eu and several oxysulphide:RE films using electron beam evaporation, RF magnetron sputtering, and a RF ion-plasma diode sputter deposition technique. The RF ion-plasma technique yielded superior results. No luminescence was reported for the films grown using electron beam evaporation. They achieved an efficiency of 1.4 lm/W and 3.06 lm/W at 8 kV and 1 μA/cm^2 for r.f. sputtered Y_2O_3:Eu and Y_2O_2S:Eu films, respectively. Hsieh et al [Hsi94] employed rf magnetron sputtering to deposit $ZnGa_2O_4$:Ga. Ouyng et al [Ouy95] also used rf sputtering to deposit Y_2O_3-SiO_2:Eu thin films. Films were grown at 300-450 °C and annealed around 1000 °C for 2 hours. Brightness values of 10-20 % that of the powder were reported.

Liquid phase epitaxy and low pressure metal-organic chemical vapor deposition were utilized by Robertson et al and West et al. Robertson et al [Rob80] deposited $Y_3Al_5O_{12}$:Ce thin films. West et al. [Wes90] did not report efficiency values for their Y_2O_3:Eu films, but showed that there was an effect of deposition parameters on the amount of active Eu in the S_6 vs C_2 sites. This was done by following the 611 nm peak (^5D_o - $^7F_2$ transition) versus the 533 nm peak ($^5D_1$ - $^7F_1$ transition).

Rao [Rao96] utilized sol-gel processing to deposit Y_2O_3:Eu thin films. Films were amorphous as-deposited at a substrate temperature of 400 °C. The films became crystalline and luminescent after a 600 °C, 2 hour anneal. The characteristic polycrystalline cubic x-ray diffraction pattern was not achieved until annealing temperatures of 800 °C. Like West et al., they showed that the crystallographic occupation of europium was influenced significantly by processing temperature.

Pulsed Laser Deposition (PLD)

More recently, pulsed laser deposition (PLD) has been used to deposit phosphor films. McLaughlin et al. [McL93] deposited ZnS:Mn thin films by PLD. Greer et al. [Gre94a] used PLD to deposit yttrium aluminum garnet

(YAG) doped with various rare earth dopants. They reported efficiencies for films from 2 to 8 μms thick. All films were annealed in oxygen between 1400 and 1650 °C for varying times. Reported were efficiencies of 3.8 lm/W for a 8 μm thick film and 2.4 lm/W for a 2 μm film at 15 kV and 25 $\mu A/cm^2$ were reported. Hirata el al. [Hir96] also deposited $ZnGa_2O_4$:Tb, $Y_3Al_5O_{12}$:Tb (YAG:Tb) and Y_2O_3:Eu using PLD. Films deposited at 300 °C were amorphous and required anneals of 800 °C or greater to establish good crystallinity and luminescence. They reported similar results for the yttria doped with europium thin films.[Hir97] No relative brightness or efficiency data were given.

The growth technique used to deposit the phosphor films was pulsed laser deposition (PLD). PLD has been used extensively as a growth technique for superconductors and other complex oxide systems.[Nar87] It is the deposition technique of choice to deposit superconducting films due to its accuracy for stoichiometry over sputtering and other growth techniques. This physical vapor deposition technique couples a focused pulsed laser onto a target where absorption and subsequent evaporation take place. Excimer lasers are normally used, varying in wavelengths from 1064 to 532, 355,or 248 nm. A main limitation of this growth technique are particulate evolution during deposition and limitation in deposition area.

Stoichiometric deposition results from the laser-target interactions. There are two basic laser-target interactions leading to ablation: surface heating and volume heating.[Sin94] In the surface heating regime, the optical absorption depth of the laser beam is much smaller than the thermal diffusion distance. During ablation, either a planar vaporization interface propagates through the bulk, or subsurface heating may occur leading to non-linear ablation characteristics. The temperature rise in this regime is governed by

$$\Delta T = \frac{(1-R)\Phi t_p}{C_v\ \rho(2Dt_p)^{1}/2}$$

where R is the reflectance, (1-R) is the amount of radiation absorbed, F is the energy density, t_p is the pulse duration, C_v is specific heat, ρ is the density and $(2Dt_p)^{1/2}$ is the thermal diffusion distance.[Sin90]

In volume heating, the optical absorption depth is much larger than the thermal diffusion distance, and the optical absorption depth is inversely proportional to the absorption coefficient, α. In this regime, sub-surface heating effects dominate and the temperature rise is governed by

$$\Delta T(z) = \frac{(1-R)\Phi\alpha\exp(-\alpha z)}{C_v\ \rho}$$

where z is the absorption depth.[Sin94, Che88] For large band gap semiconductors and dielectric materials, optical absorption can be quite high at the shorter wavelengths. This leads to high surface temperatures since high energy densities are confined to a small volume. For these materials, temperatures greater than the melting temperature are reached at depths greater than the thermal diffusion distance. Target components, therefore, cannot segregate despite differences in vapor pressures. This yields congruent evaporation from multicomponent targets.

Besides wavelength [Kor89], repetition rate [Cha90] and spot size [Wu90] also influence the ablation characteristics and therefore thin film growth. The spot size of the laser beam will affect the deposition rate and the amount of particulates ejected by the beam. Larger beams are attenuated by the plasma plume created when the laser strikes the target. As the spot size is reduced, the deposition rate increases due to reduced beam-evaporation plume interaction. The beam-plume interaction can reduce the number of particulates by evaporating them in the vapor phase.[Eye87] The reduction of laser wavelength has this same effect since there is a high absorption in the vapor plume that further volatilizes the fragments.[Kor89] It has been shown that changing the repetition rate affects the film crystallinity and morphology. Reducing the repetition rate reduces the growth rate which increases the time atoms can diffuse to equilibrium positions. This leads to a higher crystallinity and film density.[Wu90] For every set of growth conditions there will be an optimum repetition rate, or arrival rate, that yields smooth dense thin films.[Cha90] Coupled with the ability to change the standard growth parameters such as substrate temperature and growth pressure, PLD has emerged as a technique capable of depositing a wide variety of materials.[Che88]

Table 2-1 Efficiency Data for Phosphor Thin Films

Phosphor	Volts (kV)	Current Density ($\mu A/cm^2$)	Bright-ness (Cd/m^2)	Eff. (lm/W)	Growth Tech.	Ref.	Comment
ZnS:Mn	10	1	34.3	1.08	a	Cus52	also ZnS:Zn - blue
ZnS:As,P	10	1	34.3	1.08	a	Stu55	from plot
ZnS:As,P	20	1	119.9	1.88	a	Stu55	from plot
ZnS:Mn	12	10	6.9	0.02	b	Fel57b	as-deposited
ZnS:Mn	12	10	68.5	0.18	b	Fel57b	annealed
ZnS:Mn	12	10	116.5	0.31	b	Fel57b	Al coated
ZnS:Mn	12	10	342.6	0.90	b	Fel57b	annealed, fogged film
CaF_2:5%Mn	12	10	27.4	0.07	b	Fel57b	clear film
$\beta Zn_2(PO_4)_3$:3% Mn	12	10	411.1	1.09	b	Fel57b	
$CaWO_4$:W	12	10	34.3	0.09	b	Fel57b	clear
$CaWO_4$:W	12	10	68.5	0.18	b	Fel57b	fogged film
Zn_2SiO_4:8%Mn	12	10	205.6	0.54	b	Fel57b	clear
Zn_2SiO_4:8%Mn	12	10	1027.8	2.69	b	Fel57b	annealed, fogged film
$CaWO_4$:W	10	10	54.1	0.14	b	Fel57b	annealed, fogged film
α-Zn_2SiO_4:Mn	7.5	10	58.2	0.24	c	Kir61	vycor substrate

Phosphor	Volts (kV)	Current Density ($\mu A/cm^2$)	Bright-ness (Cd/m^2)	Eff. (lm/W)	Growth Tech.	Ref.	Comment
α-Zn_2SiO_4:Mn	7.5	10	75.4	0.32	c	Kir61	silica, anneal (1250 °C, 1 hr.)
α-Zn_2SiO_4:Mn	7.5	10	13.7	0.06	c	Kir61	pyrex substrate
α-Zn_2SiO_4:Mn	7.5	10	10.3	0.04	c	Kir61	pyrex substrate
α-Zn_2SiO_4:Ti	7.5	10	3.4	0.01	c	Kir61	pyrex substrate
α-Zn_2SiO_4:Ti	7.5	10	6.9	0.03	c	Kir61	silica, anneal (1000 °C, 1 hr.)
$CdSiO_3$:Mn	7.5	10	92.5	0.39	c	Kir61	silica, anneal (1150 °C, 1 hr.)
Y_2O_3:Eu	8	1	36.0	1.40	d	Bon95	sapphire
La_2O_2S:Eu	8	1	5.2	0.20	d	Bon95	sapphire
Y_2O_2S:Eu	8	1	78.0	3.10	d	Bon95	sapphire
Y_2O_2S, Gd_2O_2S:Tb	8	1	26.0	1.02	d	Bon95	sapphire
Y_2O_2S:Tb	8	1	24.0	0.94	d	Bon95	sapphire
La_2O_2S:Tb	8	1	40.0	1.60	d	Bon95	sapphire
La_2O_2S:Nd	8	1	1.2	0.05	d	Bon95	sapphire
La_2O_2S:Tb			685.2	7.37	e	Map73	0.1 W/cm^2
La_2O_2S:Tb			2000.0	2.15	e	Map73	1.0 W/cm^2

Phosphor	Volts (kV)	Current Density ($\mu A/cm^2$)	Bright-ness (Cd/m^2)	Eff. (lm/W)	Growth Tech.	Ref.	Comment
$Y_3Ga_2Al_3O_{12}$:Tb	10	25		1.60	f	Gre94	from graph, 2 μm film
$Y_3Ga_2Al_3O_{12}$:Tb	15	25		2.40	f	Gre94	from graph, 2 μm film
$Y_3Ga_2Al_3O_{12}$:Tb	10	25		2.80	f	Gre94	from graph, 8 μm film
$Y_3Ga_2Al_3O_{12}$:Tb	15	25		3.80	f	Gre94	from graph, 8 μm film

[a] Chemical Vapor deposition

[b] Thermal Vacuum Evaporation

[c] Spray Pyrolysis

[d] RF Ion-plasma Sputtering

[e] RF Magnetron Sputtering

[f] Pulsed Laser Deposition

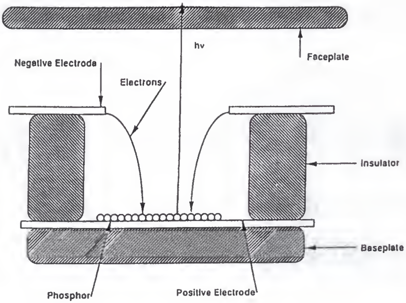

Figure 2-1. Alternative lifted edge emitter field emission display technology. Display allows for thin film phosphor integration with edge emitter onto same substrate.

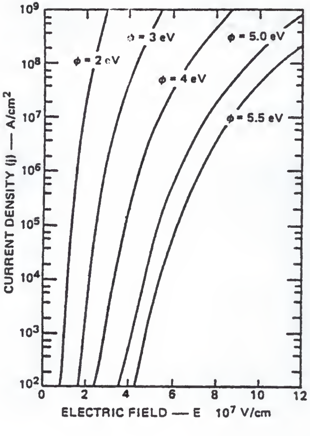

Figure 2-2. Plots of Fowler-Nordheim equation for current density, J, as a function of electric field, E, for varying work functions, Φ.[Bro92]

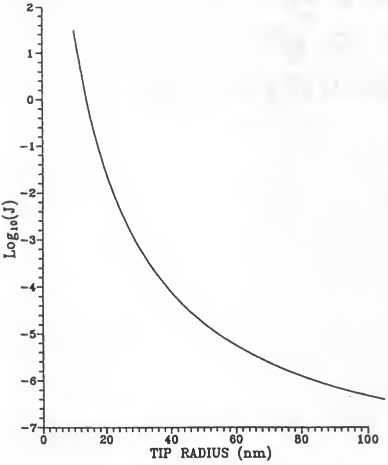

Figure 2-3. Calculated log of current density, J, plotted as a function of field emission tip radius. The applied external voltage was 30 V and the tip to anode separation distance was fixed at 20 nm.[Cut93]

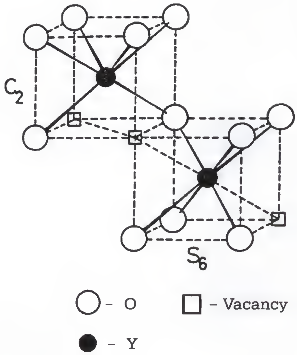

Figure 2-4. Representation of the Y_2O_3 crystal structure showing the two different cation symmetries, S_6 and C_2. In the C_2 site there is an oxygen vacancy (squares) on the face diagonal, while the S_6 site has a body diagonal oxygen vacancy pair.[Jag94] This yields chemically equivalent but crystallographically in-equivalent sites.

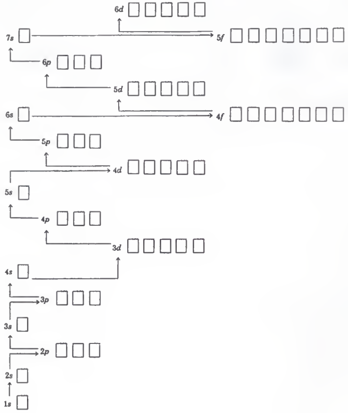

Figure 2-5. Fill order for electron sub-energy levels in solids.[Sie67]

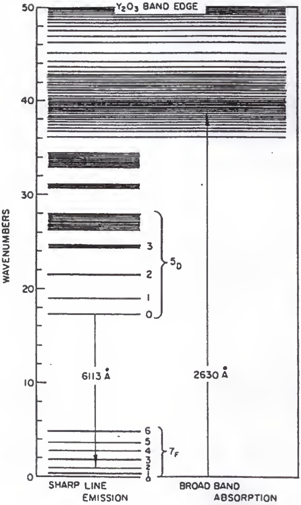

Figure 2-6. Energy level diagram for europium, Eu^{+3}, doped yttrium oxide. The characteristic emission at 611 nm results from the inter-atomic $^5D_0$-$^7F_2$ transition within the europium.[Wic64]

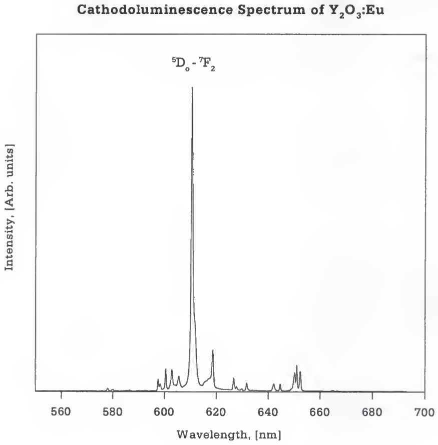

Figure 2-7. Cathodoluminescence spectra for $Y_2O_3:Eu^{+3}$ showing sharp line emission at 611 nm. Spectra taken with Oriel Multispec Spectrometer.

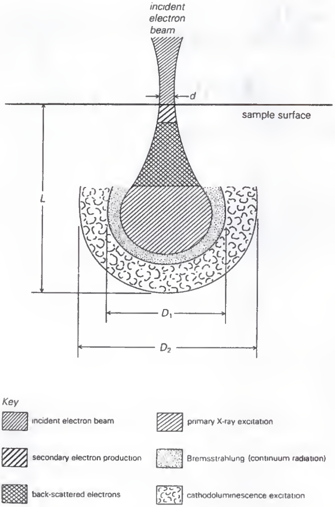

Figure 2-8. By-products produced by electron in the interaction volume, where D_1 is the X-ray generation area and D_2 is the full cathodoluminescence width after penetration and diffusion of electron-hole pairs.[Mar88]

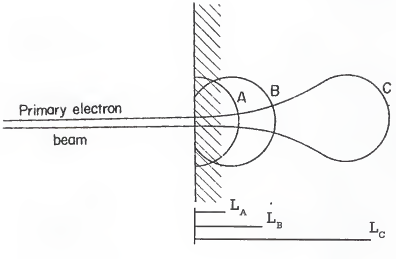

Figure 2-9. Changes in interaction volume depth and beam diameter with voltage. As the voltage is increased (A to C) the penetration depth (L_A to L_C), is increased while the cross-section of surface interaction is decreased.[Has90]

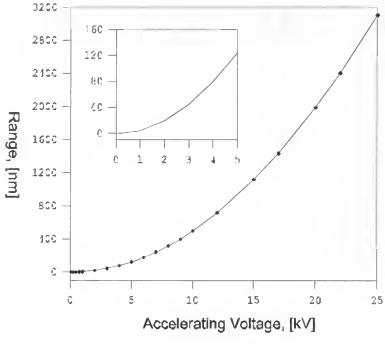

Figure 2-10. Plot of electron penetration depth versus accelerating voltage, per Terril's equation for Y_2O_3.[Fel60]

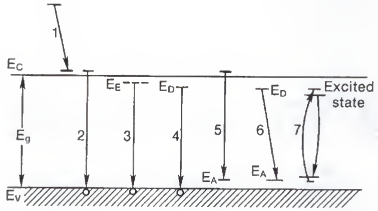

Figure 2-11. Schematic diagram of luminescence transitions between the conduction band (E_c) and the valence band (E_v). Processes 4-6 are typical transitions occurring within semiconductors where process 7 is typical for rare earth dopants.[Yac92]

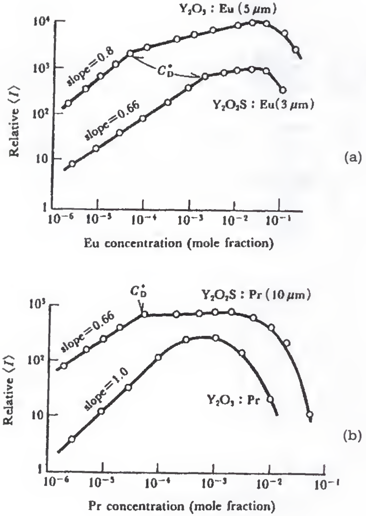

Figure 2-12. Cathodoluminesecent intensity versus activator concentration (a) Eu in two host materials displaying indirect activator excitation and (b) for Pr in two host materials displaying both direct (slope =1.0) and indirect (slope=0.66) behavior.[Oza90]

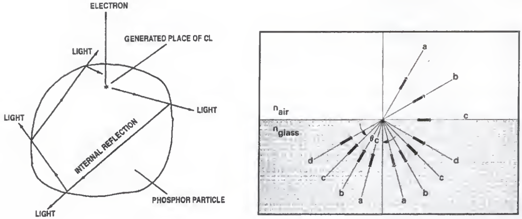

(a) (b)

Figure 2-13. Illustration of light internally reflected in (a) a powder versus, (b) a thin film. Light eventually escapes the powder, while only light within the film incident the surface at angles less than θ_c (rays a & b) will escape. Light incident at angles greater (rays c & d) is trapped within the film and will continue to reflect internally.

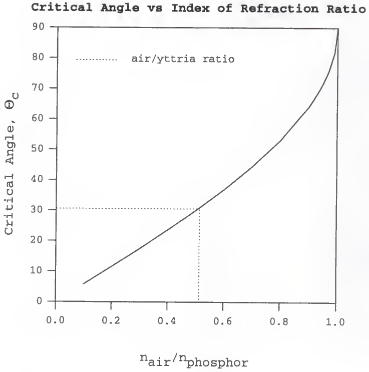

Figure 2-14. Plot of critical angle versus the refractive index of air to phosphor ratio. For Y_2O_3 at 611 nm, the index of refraction is equal to 1.93. This yields a critical angle of 31°.

CHAPTER 3

EXPERIMENTAL PROCEDURE

Substrate and Target Preparation

Yttrium oxide doped with europium thin films were deposited onto Corning 2947 glass, c-axis sapphire (Al_2O_3), quartz, and (100) silicon (Si). The glass, sapphire and the quartz substrates were cleaned using a modified RCA cleaning procedure. First, the substrates were mechanically cleaned using trichloroethylene (TCE) and a cotton swab. The substrates were then ultrasonically degreased in heated (35 °C) TCE, acetone and methanol for 5 minutes each. They were then rinsed in de-ionized (DI) water and blown dry with nitrogen gas. The same solvent cleaning procedure was employed on the silicon wafers followed by a 5 second buffered hydrogen fluoride etch and a DI rinse. The silicon substrates were then blown dry with nitrogen. Some silicon substrates were roughened prior to cleaning to examine the effect on CL brightness. Silicon carbide 600 grit paper was wetted with methanol and the substrates were roughened by random hand motion for 10 seconds.

The phosphor PLD targets were manufactured from powder supplied by Osram Sylvania (type 2342 Y_2O_3:Eu lamp phosphor). Ten weight percent of various known fluxes, such as Ag_2O and NaF, were sometimes added to assist in the sintering process. The powders were pressed into 1 inch pellets and sintered at 1400 °C in air for 24 hours. A target was also manufactured from the same powder via isostatic hot pressing by Cerac, Incorporated.

Pulsed Laser Deposition (PLD)

Films were created by PLD in a high vacuum chamber which used a Leybold Trivac mechanical pump model # D4A for rough pumping and a Pfeiffer Balzers TPU 450 H corrosive turbomolecular pump with a TCP305 controller and a MD4I diaphragm backing pump. The ultimate pressure of the system was 4×10^{-11} Torr. A KrF (λ=248 nm) 1 Watt Lambda Physik Lasertechnik LPX300 excimer laser with a pulse width of 10 nanoseconds was used. Pulse frequencies between 1 and 100 Hz were possible, but all films were deposited at 10 Hz. A schematic of the deposition chamber is shown in figure 3-1. By adjusting the lens-to-target distance, varying laser beam spots with controlled sizes were achieved. The target was also rotated to reduce the number of ablated target particles deposited on the thin film surface.[Che94b] The incident laser beam struck the target at 45° away from the surface normal, generating a plume perpendicular to the target and substrate. The substrate holder was not rotated. The distance between the target and substrate could be varied from 2.5 cm to 5 cm, but 3 cm was the most commonly used target-to-substrate distance. Typically, deposition was accomplished over 15 minutes at 500 mJ/pulse with a focused spot of 0.2 cm^2 and a pulse rate of 10 Hz. This yielded 600 pulses/minute with an energy density of 2.23 J/cm^2 per pulse or 22.3 W/pulse. A 12% loss due to absorption and reflections of the mirror, lenses, and quartz vacuum window was factored into the energy density calculation. The loss was measured using a laser power meter. The combination of target-to-substrate distance and laser conditions yielded deposition rates of 3.7 Å/pulse (36.6 Å/sec) at high vacuum conditions and 2.7 Å/pulse (26.7 Å/sec) at 600 mTorr.

Ultra high purity oxygen from compressed gas cylinders was used to grow at higher pressures. The gas was introduced into the vacuum system using a MKS model 247C mass flow controller at 80 sccm. The pressure was regulated by throttling the turbo pump, using the gate valve to achieve the desired pressure. Pressures of 10^{-6} Torr to 600 mTorr were obtained using this method.

The substrates were heated via a quartz lamp to temperatures from 150 °C to 1000 °C. A stainless steel heater plate was used as the thermal contact between the lamp and the substrate. Substrates were mounted onto the plate with silver paste. Deposition temperatures were monitored using a thermocouple in contact with the stainless steel plate via support clips. Some of the as-deposited films were furnace annealed in air for varying temperatures and times to a maximum temperature of 1450 °C in a Lindberg Blue M model # 54433 high temperature furnace.

PLD Film Characterization

The PLD films were characterized using a variety of analytical techniques including x-ray diffraction (XRD), secondary electron microscopy (SEM), atomic force microscopy (AFM), scanning and static Auger electron spectroscopy (AES), Rutherford back-scattering (RBS), secondary ion mass spectroscopy (SIMS), photoluminescence (PL), and cathodoluminescence (CL). Brief descriptions of these techniques follow.

X-ray Diffraction(XRD)

X-ray diffraction [Cul78] was the primary technique used for yttria phase and crystallinity identification. A Phillips model APD 3720 x-ray diffractometer was operated at 40 kV and 20 mA to generate Cu K_a radiation of $\lambda = 1.5406$ and 1.5444 Å. The Cu K_β was removed using a Ni filter. Diffraction spectra over the 2θ range of 10 - 90° were measured. The goniometer was scanned at 3° per minute in a continuous mode. XRD is primarily a structural characterization technique but may be used for semi-quantitative composition analysis, and determination of stress-strain, crystal size, film thickness and in special cases, quantification of defect concentrations.[Smi86] These different applications of XRD result from the ability to measure and interpret peak intensity, position and width data. The Warren-Averbach method was used to deduce the crystallite size from the FWHM data.[Cul78] The (100) peak of a silica standard obtained from the National Institute of Standards and Technology was used to quantify the data from Y_2O_3:Eu.

Atoms in a solid are capable of scattering and diffracting electrons, photons, other atoms and x-rays. Incident x-rays are either constructively or destructively diffracted. Constructive diffraction results when the atoms are aligned in a periodic fashion. The different rays reinforce rather than cancel one another as in the destructive case and a diffracted signal, or peak, is detected. This peak is also referred to as a line profile. The required atomic alignment to yield constructive interference is governed by Bragg's law

$$n\lambda = 2d_{hkl}\sin\Theta_{hkl}$$

where λ is the wavelength of incident radiation, n is a small integer (1,2,3...) and is the order of the diffracted peak, typically first order with n=1; d_{hkl} is the spacing between atomic (hkl) planes where hkl are the Miller indices of the diffracting plane of atoms, and θ is the angle between the normal of the (hkl) plane and the incident x-ray beam. [Cul78] The interplanar spacings and planes for low Miller indices are shown in figure 3-2.

Since the atomic arrangement varies for each of the seven crystal systems, the allowed diffraction from various hkl atomic planes will also vary per crystal system. Appendix B shows the allowed hkl combinations. The d spacing is a function of the plane location and the lattice parameter. In cubic systems, d_{hkl} is given by

$$d_{hkl} = \frac{a_o}{\sqrt{h^2 + k^2 + l^2}}$$

where a_o is the lattice parameter of the crystal. The resulting peak contains contributions from the sample, instrumentation error and spectral distribution. By eliminating the latter two, the profile can be manipulated to quantify crystalline defects.[Smi86] The amount of x-rays which constructively diffract is dependent on the crystallinity, therefore, a direct comparison of % crystalline can be made between samples by comparing the area under the peaks. Care must be taken to measure the same physical area and thickness for all of the samples to make meaningful comparisons of peak areas. If the sample thickness is much greater than the characteristic absorption depth of x-rays, thickness differences can be neglected. The x-ray absorption depth for yttria is 10 μm. Peak width can yield information about crystallinity and defects, and position yields information about mismatch and strain.

Scanning Electron Microscope(SEM)

Scanning electron microscopy (SEM) is a powerful tool in the characterization of surface topography and defects.[Bin92] It is capable of providing micrographs with magnification as low as 10x and as high as 300,000x resulting in images with resolutions of a few nm. A JEOL 6400 SEM with true secondary and backscatter electron detectors plus an energy dispersive x-ray spectrometer (EDS) attachment was used similar to the one pictured in figure 3-3. Primary electrons were generated from a tungsten filament by thermionic emission. The operating voltage ranged from 5 kV to 30 kV, most commonly 15 kV. Since the samples were non-conductive, they were coated with Au-Pd for imaging or carbon coated for EDS analysis. The high magnification limit for these samples was ~ 100,000x. A transmission electron microscope (TEM) was employed for higher magnification. SEM was primarily used to acquire surface morphology, cross section thickness and morphology, and grain size data.

Rutherford Backscattering Spectroscopy(RBS)

Rutherford backscattering spectroscopy (RBS) was primarily used to determine film composition and stoichiometry.[Bau92a] It is one of the few quantitative surface analysis tools available. A high voltage van de Graaf accelerator with an EDS detector at Oak Ridge National Laboratory was used.

Primary beam energies of 2.2 MeV and doses of 10^{19} atoms/cm^{-2} were typically used. RBS can detect a few parts per million (ppm) of heavy elements in a light element matrix and is insensitive to chemical bonding and matrix effects, unlike Auger electron spectroscopy (AES) and secondary ion mass spectroscopy (SIMS). RBS is routinely used for quantitative compositional analysis of thin films, layered structures and bulk specimens, surface dopant analysis, defect depth distribution , quantification of percent crystallization, and film thickness (or density).[Chu86]

Backscattering results from direct collisions between He ions and nuclei of sample atoms. The energy of the back scattered particle is a function of both the amount of energy lost due to momentum transferred during the nuclear collision plus the energy loss during collisions incoming and scattered He particle with electrons in the sample. Measuring the energy of the scattered ion gives a direct measurement of the mass of the ion, and hence mass identification. The projectile energy to incident ion energy after the elastic collision ratio (kinematic factor) is given by the equation:

$$K = E_1/E_o = \frac{(\sqrt{1-((M_1/M_2)\sin\theta)^2} + (M_1/M_2)\cos\theta)}{1 + (M_1/M_2)}$$

where M_1 is the mass of incident ion, M_2 is the mass of target atom, θ is the angle between trajectory of He ion and the angle of detector.[Chu78] See figure 3-4. Since K is a function of M_1/M_2, there is a larger energy separation for lighter elements than heavier ones due to a significantly larger amount of momentum transfer to lighter elements. This results in excellent mass resolution between light elements and between light and heavy element matrixes, but poor resolution between heavy elements. There is good mass resolution for the Y_2O_3:Eu matrix.

The probability of backscattering into a given solid angle per incident particle is referred to as the differential scattering cross section, $d\sigma/d\Omega$, where

$$\frac{d\sigma}{d\Omega} = \frac{(Z_1Z_2e^2)^2}{4E}\frac{4}{\sin^4\theta}\frac{(\sqrt{1-((M_1/M_2)\sin\theta)^2} + \cos\theta)^2}{\sqrt{1-((M_1/M_2)\sin\theta)^2}}$$

where Z_1 = atomic number of incident atom, Z_2 is the atomic number of target atom, E is the incident energy before scattering, and e is the charge. The scattering cross section is usually simplified to $(Z_1Z_2e^2)^2/4e$. Since $d\sigma/d\Omega$ is proportional to Z_2^2, larger atomic number elements are more efficient in scatterering the incident ion. In the case of a Y_2O_3:Eu matrix, even though the mass resolution is poor for heavier elements, RBS is very sensitive to the yttrium and the europium.[Chu78]

Atomic Force Microscopy(AFM)

Atomic force microscopy (AFM) belongs to the family of scanning probe microscopy (SPM).[Bin82, How93] AFM was used to quantify film roughness and other morphological details about phosphor thin film surfaces. A Digital

Instrument Nanoscope III Multimode SPM was employed in both the contact or tapping modes. The instrument was mounted on a pressurized air table to minimize vibrational noise. AFM is based on attraction and repulsion forces generated between an atomically sharp tip and the sample surface. These forces can be measured to display topological data such as roughness, grain size and step heights, as well as yield physical information such as hardness, friction, and wear strength.[Bhu95]

AFM employs atomically sharp, etched Si tips attached to a cantilever beam with resonant frequencies of 60 to 400 kHz. The beam is fabricated to have a small spring constant to allow for beam deflection. As the tip is brought close to the sample, it experiences a weak Van der Waal attractive force.[How93] The tip is drawn closer causing the electron clouds of the tip and sample to overlap which induces a repulsive electrostatic force. This force goes to zero as the distance between the atoms reaches a few Å. When the Van der Waals force becomes repulsive, the tip is in contact with the sample, [How93] as shown in figure 3-5. The repulsive Van der Waal force slope is very steep in this regime and counteracts any force that attempts to push the sample and tip atoms closer together.

In the contact mode, the AFM is operated in the repulsive force regime shown in figure 3-5. Since the slope of the (+) force side is steep, changes in the Z height causes the cantilever to deflect instead of propelling the tip further into the sample. In the non-contact (tapping) mode, the AFM operates in the (-) Van der Waals (attractive) force regime where the space between the tip and the sample surface is on the order of tens to hundreds of Å. The cantilever beam is oscillated (or tapped up and down) relative to the surface, and changes in the average Z height are detected to keep a constant modulation force on the surface. The non-contact mode is more sensitive than the contact mode.

With the Digital Nanoscope, both techniques utilize a laser to detect the deflection. As pictured in figure 3-6, a laser beam is positioned on the tip at the end of the cantilever. This beam is reflected off the cantilever and into a position sensitive photo-diode detector where sub-angstrom movement can be detected.[Bhu95] The x-y position is fed back to keep the cantilever level while the deflection or height change is recorded.

To optimize the images or quantify data from AFM, the artifacts in data from scanning characteristics and noise must be removed. The Digital Nanoscope Instrument plane-fit-data-filter (3rd order) and a flatten-data-filter (0th order) were used to eliminate scanner artifacts. Vibration induced noise was erased using a scan-line-filter. This produced an image from data averaging over the nearest points. Over-compensation from repeated use of scan line filtering can introduce extra error,

Roughness, or the change in Z height, was the primary quantitative data gathered. The roughness (R_q), also called root mean square roughness (RMS), is given by

$$R_q = \sqrt{\frac{\sum (Z_i - Z_{ave})^2}{N}} \quad [\mathit{unit\ of\ length}]$$

where Z_i is the surface height, Z_{ave} is the average height displacements and N is the number of data points.

Auger Electron Spectroscopy(AES)

Auger electron spectroscopy (AES) was done using a PHI model 660 scanning Auger microprobe to identify surface contaminants and changes in the oxygen to yttrium ratio as a function of deposition and/or annealing conditions.[Hol80] The Auger process results from the excitation a of core level electron and compensation by the ejection and de-excitation of electrons possessing characteristic energies.[Str92] AES utilizes energetic electrons to initiate this process. Since Auger electrons are low energy electrons, only those from a shallow depth from the surface will survive without inelastic collisions to be detected, hence AES is a surface sensitive technique (5 - 30 Å). AES is widely used as a surface sensitive technique capable of providing elemental composition and some information on surface chemical bonding.

AES survey spectra were taken on the samples as-received and after the surface was cleaned for 1 minute by sputtering with an energetic 3keV Ar^+ beam. This time was equivalent to the removal of ~ 100 Å. Depth profiles were also done by recording the AES spectrum, sputter for 2 minutes, and record a new spectrum to detect changes in element concentrations.

Photoluminescence(PL)

Photoluminescence (PL) brightness was measured using a UVP UVG54 6 watt UV lamp and a Photo Research Pritchard 650 (PR650) camera.[Col92] This camera was equipped with an internal light source and brightness could be measured in footlamberts (fL). Instead of using peak height intensity as the brightness value, the PR650 used the calculated area-under-the-curve between 380 and 780 nm. The PR650 also determined CIE coordinates from the measured spectral distribution. The UV lamp consisted of a mercury vapor tube with filters to pass primarily the short wavelength of 254 nm (figure 3-7). The lamp intensity was 2250 $\mu W/cm^2$ at 254 nm at a distance of 3 inches. The phosphor absorbed the radiation by promoting an electron from the ground state to an excited state. The excited atom then relaxed radiatively emitting a characteristic photon.[Col92]

The lamp and the spectrometer were 90° apart, therefore samples were arranged at 45° from the lamp and the PR650. The spectrometer was focused using focal lenses. The PR650 had a resolution of 5 nm, therefore it did not resolve the true line width of the Eu^{+3} but was sufficient for peak identification and brightness comparisons. The samples were mounted on a black background to reduce reflection. Since the primary data collected were from films on silicon, PL was recorded in the reflectance mode at room temperature. More complicated PL equipment may allow spectral analysis at cryogenic temperatures, PL excitation spectroscopy, time-resolved PL, and PL mapping.[Col92, Gui95]

Cathodoluminescence(CL)

Cathodoluminescence (CL) utilizes energetic electrons to excite radiative relaxation.[Yac92] CL data was taken using two different systems. The first system used the co-axial electron gun from a PHI model 545 scanning Auger electron spectrometer with an Oriel Multispec optical spectrometer and a CCD array detector. The AES gun was capable of providing a primary electron beam with an energy from 100 eV to 5 keV and currents between 1 and 5 μA with a spot size from 0.5 to 3 mm. This resulted in DC current densities from 10 to 510 μA/cm^2.

The other CL system consisted of a EGPS-7H Kimball Physik electron gun, and an optical fiber coupled to an Ocean Optics S2000 spectrometer with a CCD array detector. The EGPS-7H electron gun was capable of energies from 50 to 5 keV and curents from 0.01 to 500 μA with spot sizes from 2 mm to 3 cm. This yielded current densities ranging from 1.4 x 10^{-3} to 1.6 x 10^4 μA/cm^2.

Both the Oriel and the Ocean Optics spectrometers were able to resolve the characteristic Eu^{+3} line emission since their resolution was less than 1 nm. The sample current was determined by biasing the electrically isolated sample carousel with a +90 volt battery with an ammeter in series to ground. The bias collected the true secondary electrons to avoid error upon secondary electron emission.

From the current density, incident power, and brightness, the efficiency can be calculate. Efficiency is given by

$$Efficiency = 100 * \pi \frac{B}{V * I_{density}} \quad [lm/W]$$

where B is the brightness [cd/m^2], V is the voltage [V], and $I_{density}$ is the current density [μA/cm^2] measured from the sample current and beam spot size. Since neither spectrometers had an internal brightness standard, intensity was measured in arbitrary units and calibrated using phosphor standards. Brightness values from phosphor standards were used to calculate absolute efficiencies. Efficiency versus accelerating voltage curves for standard phosphors were provided by the Phosphor Technology Center of Excellence (PTCOE). Data given for 1 μA/cm^2 densities. The PR650 was used to measure brightness values in cd/m^2 and chromaticity values (x,y).

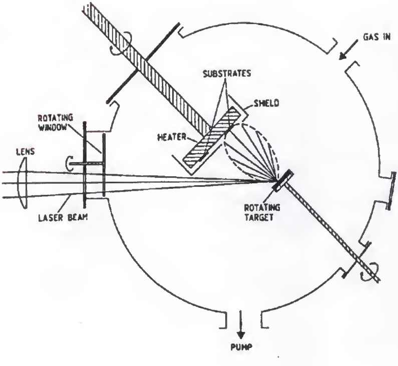

Figure 3-1. Schematic of pulsed laser deposition chamber.

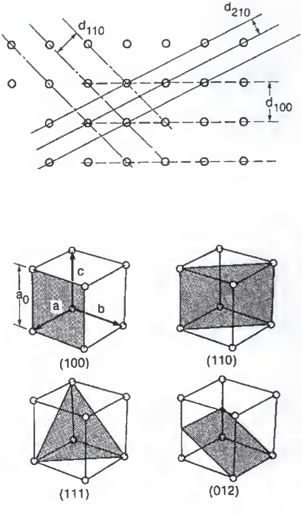

Figure 3-2. Example of x-rays being diffracted by aligned atoms in a cubic orientation. This shows the proper miller indices (hkl)for different atom locations where a_o represents the lattice parameter.[Ton92]

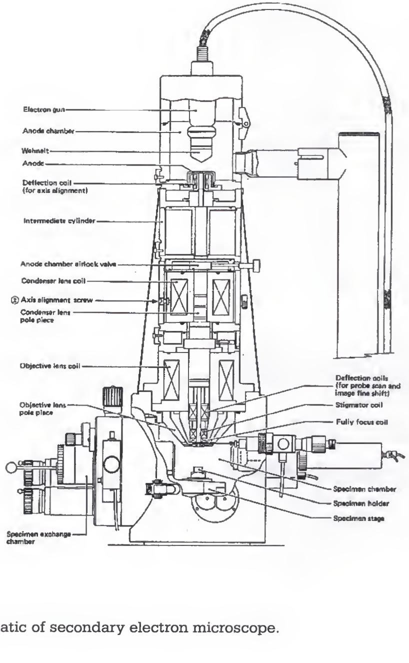

Figure 3-3. Schematic of secondary electron microscope.

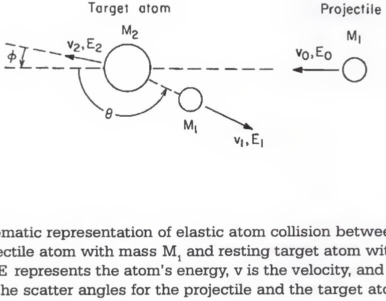

Figure 3-4. Schematic representation of elastic atom collision between projectile atom with mass M_1 and resting target atom with mass M_2. E represents the atom's energy, v is the velocity, and θ and ϕ are the scatter angles for the projectile and the target atoms, respectively.[Chu78]

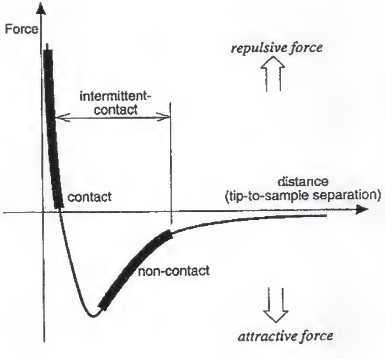

Figure 3-5. Interatomic force versus atomic distance curve illustrating the two AFM regimes, contact and non-contact.[How93]

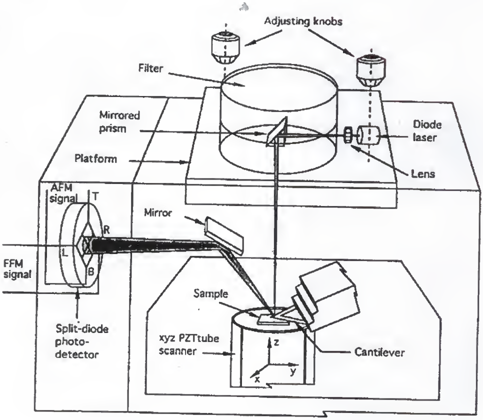

Figure 3-6. Schematic diagram of AFM utilizing position sensitive photo-diode detector to measure changes in laser position which correlates to z height changes.[Bhu95]

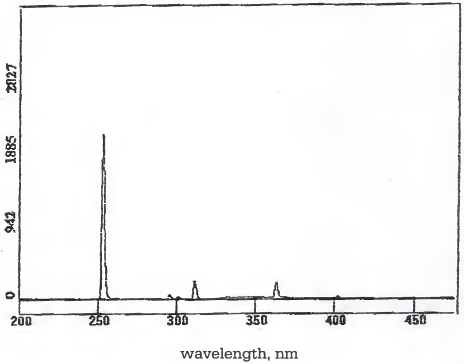

Figure 3-7. Spectrum after filtering yielding short wave UV emission.

CHAPTER 4

RESULTS

In this chapter, microstructure and chemical data are presented for Y_2O_3:Eu films grown by PLD. The objective of this study was to determine the effects of roughness on the light out-coupling in europium doped yttria thin films. It was found that increased surface roughness increased the out-coupling. The increase in roughness was accomplished in-situ by increasing the O_2 growth pressure. Samples were categorized as smooth versus rough as determined by Atomic Force Microscopy (AFM). Smooth films had RMS roughnesses of 3 nm, while rough films had RMS roughnesses of 71 nm. Luminescence data reported under PL and CL are presented first with the film growth and annealing processes resulting in these improvements following. Parameters such as deposition temperature, and annealing temperature also had a significant effect PL and CL brightness.

Photoluminescence(PL)

The films yielded weak luminescence detectable only by eye at growth temperatures of 250 °C in vacuum. The PR650 camera was able to detect emission consistently for films grown at 600 °C or higher. Films grown at 800 °C were much brighter than those deposited at 600 °C, showing that growth temperature had a significant effect on luminescence properties (figure 4-1). This effect of increasing the temperature to 800 °C from 600 °C was even greater than the effect of mechanical roughening of the substrate prior to growth, as illustrated in figure 4-2. This mechanical roughening step is discussed in further detail below.

In addition to increasing temperature, the PL response also increased as the oxygen growth pressure was increased as shown in figure 4-3. Increasing O_2 pressure above 200 mTorr increased the surface roughness from 3 nm to 71 nm, as discussed below. There was a 7 times improvement in PL brightness, corresponding to an increase to 8% the brightness of the powder standard.

Films were annealed to improve the crystallinity and further activate the europium dopant. Smooth films (grown at 100 mTorr) and rough films (grown at 600 mTorr) grown on (100) silicon at 460 °C were annealed from 600 °C to 1200 °C for 1 hour in air. Under PL, the films grown at 100 mTorr O_2 pressure did not yield detectable PL until annealed at 1000 °C, where the response was 1.81 fL after a 1200 °C anneal for 60 minutes versus 4.55 fL for an annealed film grown at 600 mTorr (figure 4-4). As seen in figure 4-4, increasing annealing temperature from 1000 °C to 1200 °C had a significant effect on PL intensity.

There was also an increase in PL intensity as the film thicknesses were changed from 0.5 μm to 9 μm (figure 4-5) at 600 mTorr and 600 °C.

Cathodoluminescence(CL)

Cathodoluminescence data were collected at a current density of 1 μA/cm^2. Figure 4-6 shows the brightness versus voltage (BV) curves for the Osram Sylvania Y_2O_3:Eu powder used as starting material for this study. Brightness data was taken with both spectrometer systems described previously. Since the power density was known, efficiency values were obtained as shown in figure 4-7. The efficiency curves had the characteristic linear and saturation regions at low and high power densities, respectively. The change from linear to saturation behavior occurred between 1.5 and 2 kV.

The CL brightness from the thin films was not detectable until they had been grown or annealed at temperatures greater than 800 °C, although the films were photoluminescent at temperatures of 450 °C (figures 4-1 to 4-3). For 800 °C deposition, the CL brightness values were low but detectable as shown in figure 4-8. The BV curves (figure 4-9) for a smooth film grown at 100 mTorr and 460 °C then annealed at 800 °C, 1000 °C, and 1200 °C in air for 1 hour show that brightness and efficiency increased as the annealing temperature was increased. There was a significant change from 1000 °C to 1200 °C. Figure 4-10 shows that annealing also increased the CL intensity from rough films grown at 600 mTorr and 460 °C. Under cathodoluminescence, the rougher films were significantly brighter than smooth films, similar to PL data (figure 4-4). The significant improvement from annealing temperature 1000 °C to 1200 °C was also similar (figures 4-4, 4-9, and 4-10)

A comparison of CL efficiency for films grown at 460 °C in either 100 mTorr or 600 mTorr and annealed at 1200 °C for 1 hour in air is shown in figure 4-11. From AFM, the RMS roughness for films grown at 100 mTorr and 600 mTorr were 3 nm and 71 nm, respectively. The films grown at 600 mTorr were ~ 3 times more efficient.

The effect of surface roughness versus CL efficiency was also demonstrated by films deposited on c-axis sapphire. Films were grown on c-axis sapphire at 800 °C, 2 x10^{-5} Torr versus 600 °C, 600 mTorr and annealed at 1200 °C in air for 60 minutes (figure 4-12). The smooth as-deposited films and smooth annealed films (grown at 2 x 10^{-5} Torr) had similar CL efficiency values, while the rough film (grown at 600 mTorr) had a significantly higher CL value. The rougher films were~ 3 times more efficient.

Films grown at a higher growth pressure than 600 mTorr (up to 6 Torr) were also annealed at 1200 °C in air for 1 hour. The efficiency was not significantly higher than those grown at 600 mTorr as shown by the efficiency data in figure 4-13.

Cathodoluminescence efficiency versus annealed film thickness was measured as shown in figures 4-14 and 4-15. Just as for PL, increased film thickness led to better CL efficiencies. The CL efficiency data for 2 kV electrons are shown in figure 4-15 for thicknesses ranging from 0.6 to 9 μm.

Thin Film Growth

The results of thin fim growth are presented below starting with the raw materials processing. The europium doped yttria powder had the characteristic cubic Y_2O_3 structure and was a perfect match for the JCPDS 25-1200 file. As-received powder pressed into targets and sintered at 1400 °C for 24 hours also displayed the cubic structure (see figure 4-16).

Films were deposited at growth temperatures of 250 °C to 800 °C in 2 x 10^{-5} Torr. Yttria was successfully grown at temperatures as low as 250 °C, regardless of substrate material. As seen in figure 4-17, there was a small (111) peak for films grown on glass substrates at 250 °C. The (111) direction remained the preferred orientation as the temperature was increased to 600 °C. There were additional peaks from films grown at 600 °C resulting from grains aligned in other directions. Similar results were seen for films grown on (100) silicon and c-axis Al_2O_3 (sapphire), as shown in figures 4-18 and 4-19, respectively. It is noted that for the yttrium oxide/silicon system, the (100) silicon peak was at 69°, which, for clarity, is not plotted on these graphs. There were also small silicon K_β and K_α peaks present at 61° and 32° in some of the XRD plots.

As the growth temperature was increased, the FWHM for the (111) peak changed with temperature as shown by figure 4-20. A poorly crystalline polycrystalline pattern was observed for films grown at 250 °C on all substrates, yielding a high FWHM of 0.383. The crystallinity improved, changing to a strong (111) texture at temperatures greater than 250 °C, corresponding to a decrease in FWHM. At 800 °C, the films on silicon and sapphire transformed back from highly (111) texture to a polycrystalline film resulting in an increase in the FWHM.

There was also a corresponding change in film morphology with the change in crystal structure and texture. The typical thin film morphology was smooth (figure 4-21) for films grown at pressures less than 1×10^{-4} Torr on the (100) silicon substrates. Particulates ranging from 0.125 to 0.25 μm seen in figure 4-21 resulted from the ablation process. Particles from the target were liberated as a result of the absorption and melting processes during ablation and could be reduced by using denser targets, reducing the laser energy density during ablation or by utilizing some of the other particulate reduction schemes developed recently.[Che94b] As seen in the cross-section SEM photograph (figure 4-22), the growth process yielded nice columnar grains. As the growth temperature was increased for deposition on (100) silicon at 2×10^{-5} Torr, the films first became smoother from 250 °C to 400 °C, then more granular from 400 °C to 800 °C, as seen by figures 4-23 to 4-25.

X-ray diffraction data were complemented with chemical analysis using AES, RBS and SIMS. Figure 4-26 shows a typical Auger spectrum from a yttria film deposited on (100) silicon at 600 °C at 10^{-5} Torr, after cleaning the near surface with Ar^+ sputtering for 1 minute. The surface of the as-received samples was contaminated with carbon (272 eV) and chlorine (181 eV) peaks, which is normally seen. Yttrium Auger peaks were detected at 75, 106,122, 1743 and 1817 eV. From the AES handbook, the low energy triplets were expected to be at 77, 110, and 127 eV. The expected higher energy peaks are at 1746 and 1821 eV. The oxygen peak was seen at 509 eV while 510 eV is characteristic energy. The expected theoretical values are for the Y metal and the differences in detected peak energies and theoretical values result from chemical shifts in forming the Y_2O_3 solid. The small peak at 215 eV resulted from argon implantation from the Ar^+ sputtering. Europium was not detected due to its low concentration in Y_2O_3. Europium's characteristic Auger peaks are located at 109, 139 and 858 eV, but no signal was detected at 858 eV.

Surface Roughening

The effect of surface roughening was initially investigated by growing europium doped yttria on smooth and mechanically roughened substrates. The substrates were roughened prior to growth with 600 grit SiC paper as described previously. As in figure 4-27, yttria was successfully deposited onto the roughened substrate with a morphology indistinguishable from the substrate.

The goal of changing surface roughness in-situ was accomplished by increasing the O_2 growth pressure. The crystalline texture changed as a function of the growth pressure (figure 4-28), as it did with temperature (figure 4-18). The films transformed from preferred (111) orientation at low O_2 pressure to more random polycrystalline at pressures greater than 400 mTorr. As seen in figure 4-28, at 600 mTorr the (400) peak becomes very pronounced. The (111) FWHM is plotted versus O_2 pressure during growth in figure 4-29, showing that the FWHM decreased as the pressure was increased up to 200 mTorr. Above this pressure, the reported FWHM increased again. As seen in figure 4-28, pressures above 200 mTorr resulted in a change from preferential (111) orientation to more random polycrystalline films. Just as with increasing growth temperature (figure 4-20), as the film changed from a (111) preferred orientation to a random polycrystalline film, the FWHM increased.

At 600 mTorr and 600 °C, the peaks marked (*) in figure 4-28 were from a yttrium silicate phase that formed during deposition. To avoid reactions between Y_2O_3 and SiO_2 to form a silicate, a nucleation layer of Y_2O_3 was deposited at 200 mTorr for two minutes prior to continued deposition at 600 mTorr. As seen in figure 4-30, formation of a silicate phase was avoided and a preferential (111) orientation was maintained by using this nucleation layer.

The change from a preferential (111) texture to a random polycrystalline one was also evident from SEM photographs. Figures 4-31 to 4-36 show the change in morphology as the oxygen pressure was increased. The morphology became nodular in nature and rougher as the pressure was increased from 0.2 mTorr (figure 4-31) to 600 mTorr (figures 4-35 and 4-36). The nodule size, as well as the grain size, were well below 1 μm. The nodule size varied from 100 ± 15 nm for films grown at 400 mTorr and 80 ± 15 nm for films grown at 600 mTorr (figure 4-36). This change in structure and nodule size is seen in figure 4-37, where the O_2 pressure was increased from 0.05 mTorr to 80 mTorr, 600 mTorr, and then 1 Torr.

A change in film morphology was also apparent from AFM measurements of the RMS roughness of surfaces versus oxygen pressure during growth (figure 4-38). The RMS roughness, increased from 2 nm to 71 nm as the O_2 pressure was increased from 0.02 to 600 mTorr.

Film thickness, at a fixed O_2 pressure and temperature, was also varied by controlling the deposition time. As expected, the growth was linear with respect to deposition time as seen in figure 4-39, which shows film thickness versus growth time for films grown at 600 °C and 600 mTorr on (100) silicon. The columnar growth was maintained even at these long growth times (figure 4-40).

The Y/O peak heights were compared using AES to determine if there was any change in oxygen content with increasing oxygen pressure during deposition. The change in Y/O peak height ratios is seen in figure 4-41. The pressed target had a Y/O ratio of 14. According to figure 4-41, this would correspond to a film grown in O_2 pressures between 100 and 200 mTorr. RBS data were collected from samples grown at 100 mTorr and 600 °C to quantify the Y, O and Eu composition (figure 4-42). The broad plateau from 0.7 to 1.275 MeV originated from scattering from the silicon substrate. Using a fitting routine, the composition was determined to be $Y_{0.367}O_{0.626}Eu_{0.007}$. RBS data were also collected from samples grown at 600 mTorr and 600 °C. At 600 mTorr and 600 °C, films grown on (100) silicon were to rough to accurately analyze with RBS.

Figure 4-43 shows a typical SIMS profile from films deposited at 100 mTorr and 600 °C. Oxygen was detected at a mass/charge ratio of 16, while yttrium was detected at 89 and europium at 151 and 153.

Annealing

Samples were annealed to improve the crystallinity and determine the effects on the luminescence brightness. The effect of annealing on the crystal structure is shown by the XRD patterns of figures 4-44 through 4-47. Figure 4-44 shows the change in crystal structure for films grown at 600 mTorr and 460 °C, then annealed at 800 °C, 1000 °C, and 1200 °C for 1 hour in air. The films remained polycrystalline, but an interfacial reaction was detected at 1000 °C that converted the silicon/yttrium oxide to a yttrium silicate phase. The α-$Y_2Si_2O_7$ phase was the best fit. Figure 4-45 shows that annealing reduced the FWHM from 0.51° to 0.14° as the annealing temperature was increased from 460 °C growth temperatures up to 1200 °C annealing temperatures. Films grown at 100 mTorr at 460 °C (figure 4-46) were (111) oriented and remained textured for all annealing temperatures. The (111) FWHM (figure 4-47) decreased from 0.18° to 0.13°, a value similar to the film grown at 600 mTorr and annealed at 1200 °C. The (111) FWHM value for the powder was even lower, ranging from 0.096° to 0.11°.

The nodule size increased with annealing temperature as shown by figure 4-48. The sample was deposited at 600 mTorr and 600 °C on (100) silicon (figure 4-48a) followed by furnace annealing at 1000 °C for 30 minutes in air (figure 4-48b). Grains increased from 80 ±15 nm to 100 ± 20 nm in size. This size of nodules was still an order of magnitude smaller than that of phosphor powder particles at 5 μm.

RBS data from a film grown at 100 mTorr, 600 °C and annealed at 1000 °C for 30 minutes in air is shown in figure 4-49. The composition of the film was the same prior to and after annealing. However, there was an interfacial reaction with the silicon substrate resulting in a yttrium rich silicate phase. This can be seen as a change in the low energy edges of the peaks for oxygen and yttrium and for the high energy edge of Si. The fit routine yielded the same composition for the annealed film as for the as-deposited condition.

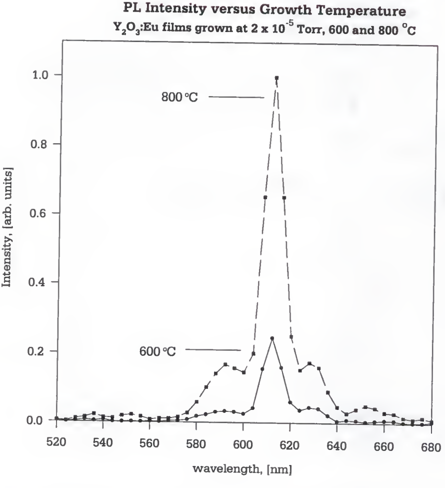

Figure 4-1. Photoluminescence versus growth temperature showing an increase in intensity as temperature is increased. Films grown on (100) silicon at 600 and 800 °C at 2 x 10^{-5} Torr.

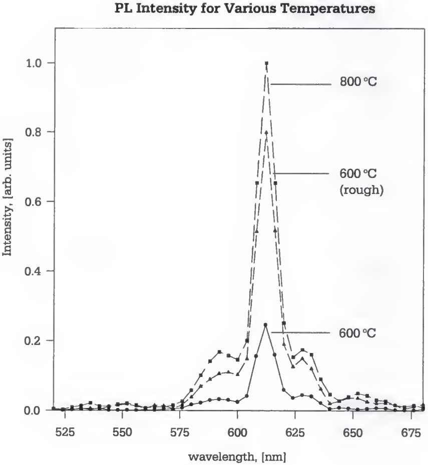

Figure 4-2. Photoluminescence versus temperature for film grown at 600 and 800 °C compared to a film deposited on a mechanically roughened silicon substrate at 600 °C. Substrate was roughened with 600 grit SiC paper prior to deposition.

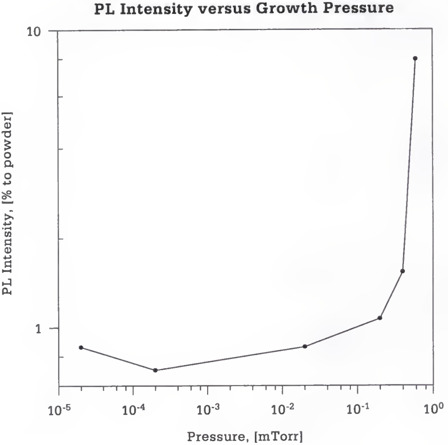

Figure 4-3. Photoluminescence versus O_2 growth pressure showing an increase in PL intensity beginning at 200 mTorr. Films grown on (100) silicon at 600 °C. Films were 1 µm thick.

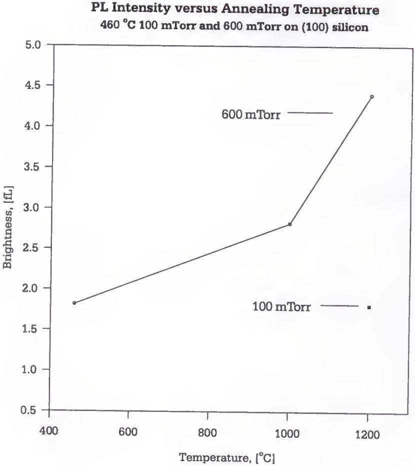

Figure 4-4. Photoluminescence versus annealing temperature showing increase in PL intensity as the annealing temperature was increased. Rough film grown at 600 mTorr, 460 °C and annealed at 1200 °C is approximately 3 times brighter than smooth film grown at 100 mTorr, 460 °C and annealed at 1200 °C. Films were annealed for 60 minutes in air.

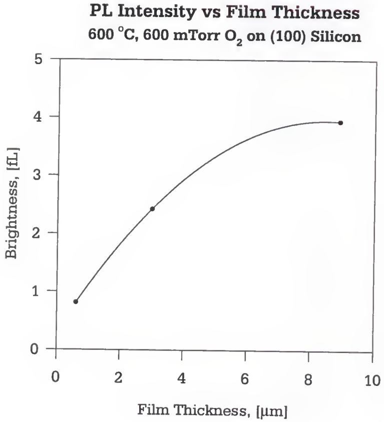

Figure 4-5. Photoluminescence versus Y_2O_3:Eu film thickness showing an increase in PL intensity as film thickness was increased. Films grown on (100) silicon at 600 mTorr and 600 °C.

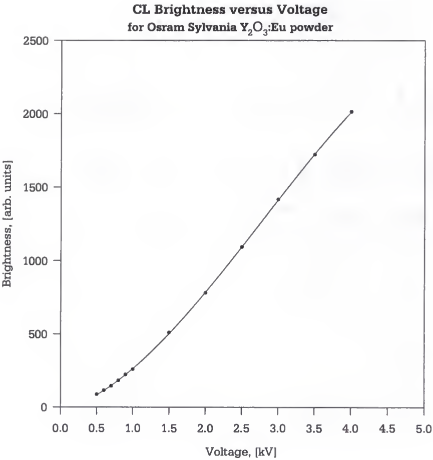

Figure 4-6. Cathodoluminescence brightness versus voltage for Osram Sylvania standard powder at 1.0 μA/cm² current density.

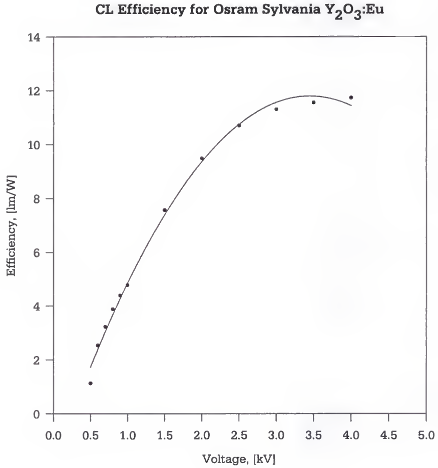

Figure 4-7. Cathodoluminescence efficiency of Osram Sylvania powder standard at 1 μA/cm^2 versus applied voltage. Shows characteristic linear low voltage region with saturation at higher power density at around 2.5 kV.

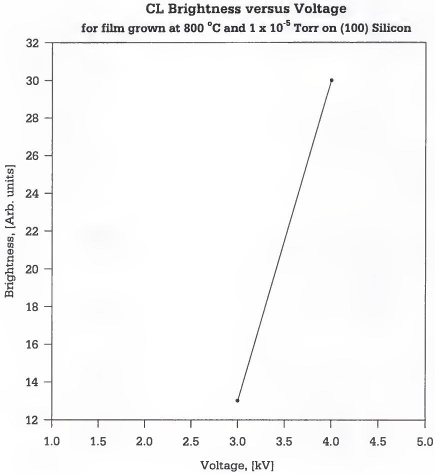

Figure 4-8. Brightness versus voltage for film grown at 800 °C on (100) silicon at 2 x 10^{-5} Torr. Data taken at 1 μA/cm^2.

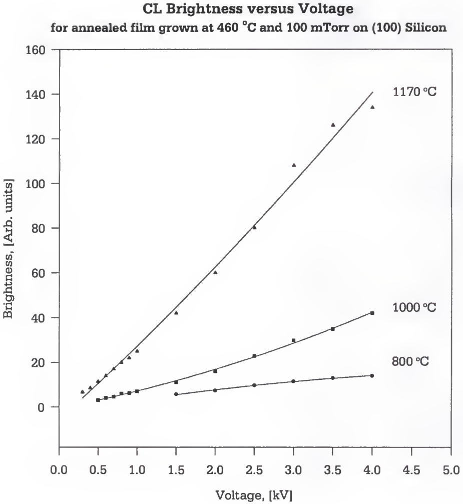

Figure 4-9. Brightness of film grown at 460 °C, 100 mTorr of O_2 pressure and annealed at 800, 1000, and 1170 °C for 1 hour in air. The films grown at 460 and 600 °C did not have detectable cathodoluminescence.

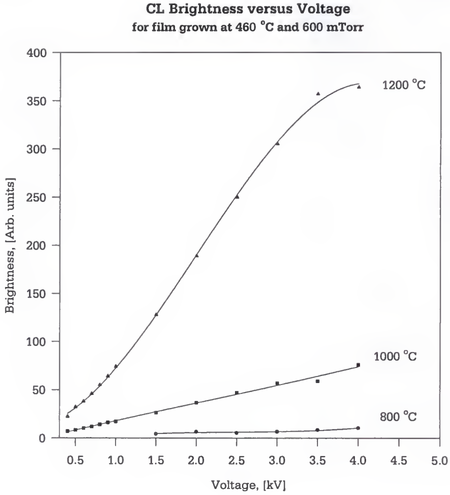

Figure 4-10. Brightness of film grown at 460 °C, 600 mTorr of O_2 pressure and annealed at 800, 1000, and 1170 °C for 1 hour in air. The films grown at 460 and 600 °C did not have detectable cathodoluminescence.

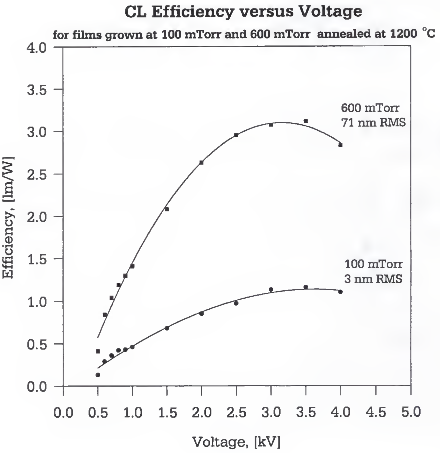

Figure 4-11. Cathodoluminescence efficiency of films grown on (100) Si at 460 °C and 100 mTorr versus 600 mTorr. Efficiency taken at 1 μA/cm^2. Typical RMS values of 3 nm and 71 nm were obtained at 100 mTorr and 600 mTorr, respectively.

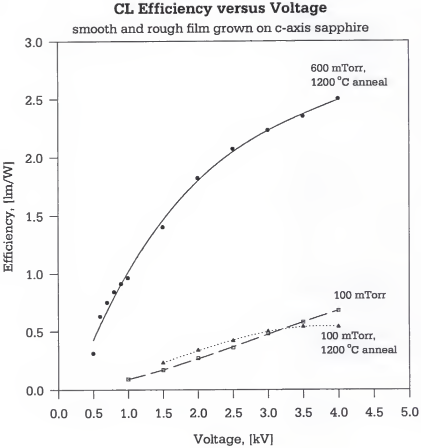

Figure 4-12. Cathodoluminescence efficiency versus voltage for Y_2O_3:Eu deposited onto c-axis sapphire. Rough annealed film grown at 600 °C and 600 mTorr is approximately 3 times more efficient than smooth annealed films grown at 800 °C at 2×10^{-5} Torr. Films were annealed at 1200 °C in air for 60 minutes. Data taken at 1 $\mu A/cm^2$.

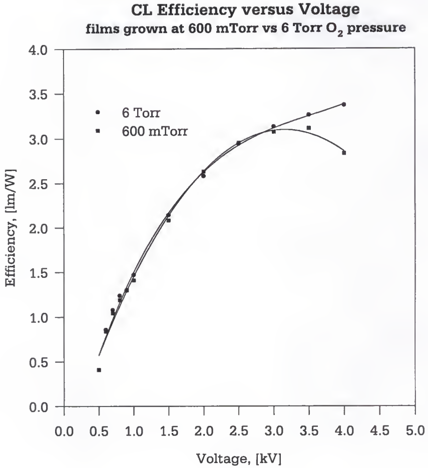

Figure 4-13. Plot of cathodoluminescence efficiency versus voltage as O_2 pressure is increased from 600 mTorr to 6 Torr. Films were grown on (100) Si at 460 °C and annealed in air at 1200 °C for 1 hour. Efficiency data taken at 1 μA/cm^2.

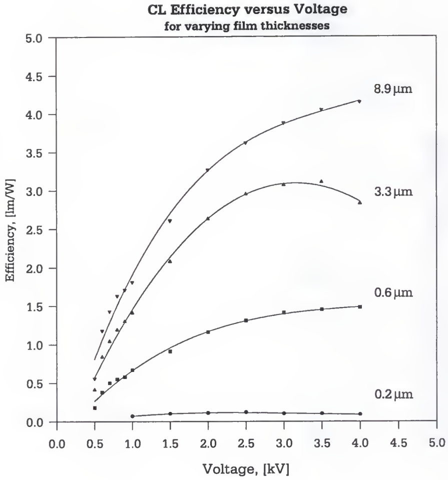

Figure 4-14. Cathodoluminescence versus voltage for increasing thin film thicknesses taken at 1 $\mu A/cm^2$. Films grown on (100) Si at 600 °C, 600 mTorr oxygen growth pressure and annealed in air at 1200 °C for 1 hour.

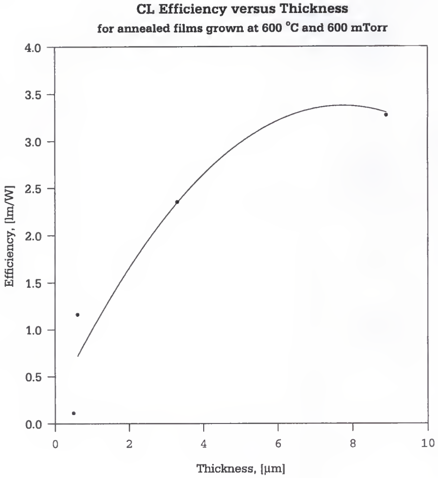

Figure 4-15. Cathodoluminescence efficiency as a function of film thickness for films grown on (100) Si at 600 °C, 600 mTorr and annealed in air at 1200 °C for 1 hour. Electron beam conditions were 2 kV and 1 μA/cm^2.

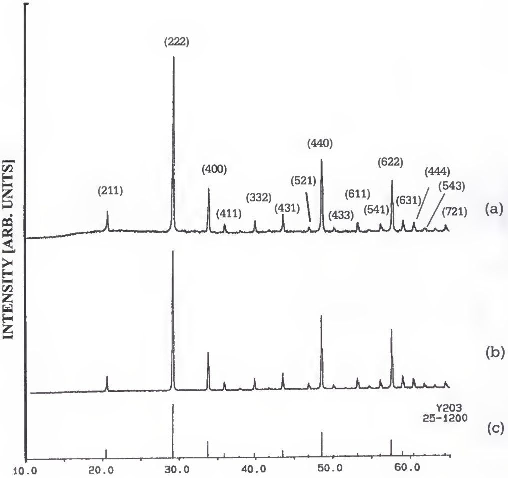

Figure 4-16. X-ray diffraction patterns of (a) yttria ablation target pressed from (b) Osram Sylvania ytrria powder doped with 4.5 weight percent Eu and (c) the cubic yttria JCPDS file 25-1200.

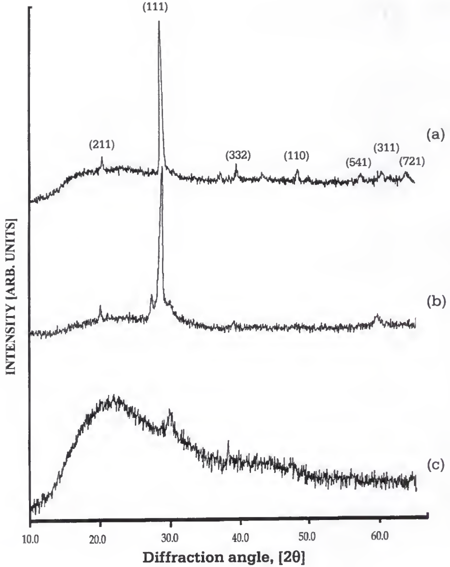

Figure 4-17. X-ray diffraction patterns of yttria grown on glass substrates for (a) 600 °C, (b) 400 °C, and (c) 250 °C at 2×10^{-5} Torr.

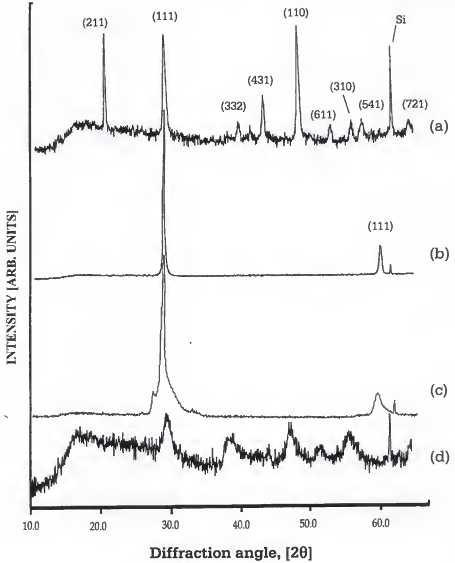

Figure 4-18. X-ray diffraction patterns of yttria films grown on (100) silicon at (a) 800 °C, (b) 600 °C, (c) 400 °C, and (d) 250 °C at 2 x 10^{-5} Torr.

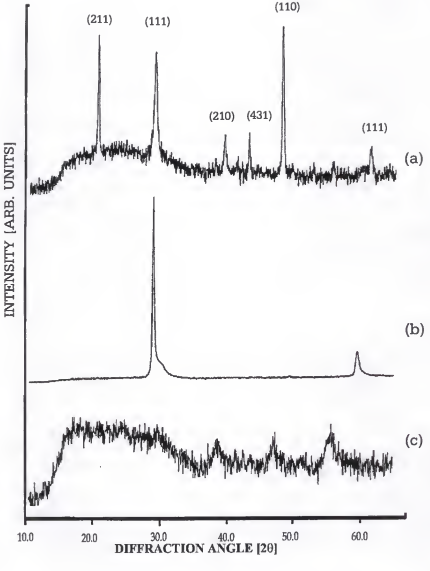

Figure 4-19. X-ray diffraction patterns for yttria films grown on c-axis sapphire for (a) 800 °C, (b) 600 °C, and (c) 250 °C at 2×10^{-5} Torr.

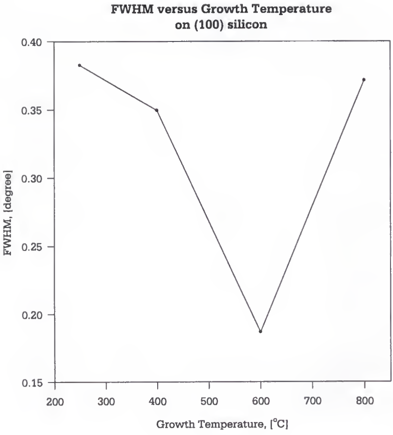

Figure 4-20. FWHM versus growth temperature for films grown on (100) silicon at 2×10^{-5} Torr.

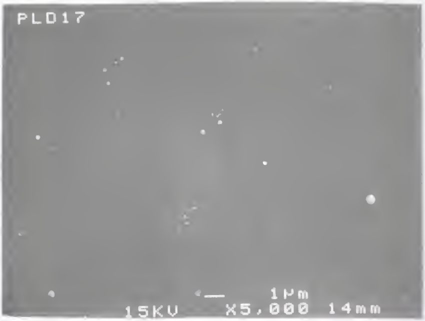

Figure 4-21. SEM photograph of film grown at 2×10^{-5} Torr at 600 °C on (100) silicon.

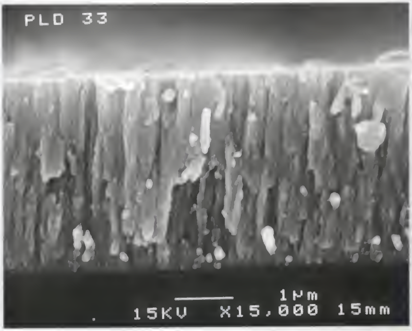

Figure 4-22. SEM cross-section photograph showing columnar grain structure for Y_2O_3:Eu deposited on (100) silicon at 2 x 10^{-5} Torr at 600 °C.

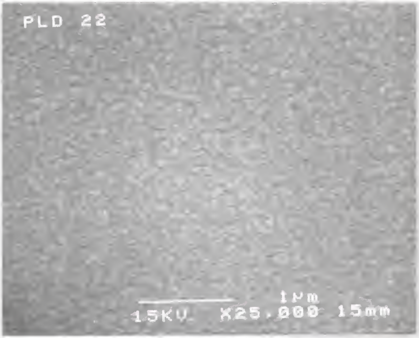

Figure 4-23. SEM photograph of Y_2O_3:Eu film deposited on (100) silicon at 250 °C at 2×10^{-5} Torr.

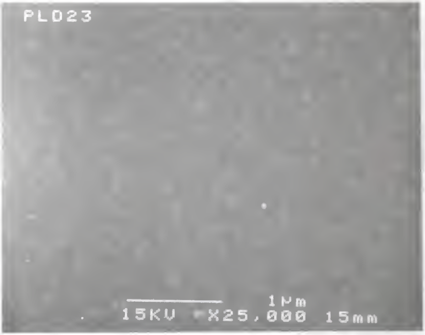

Figure 4-24. SEM photograph of Y_2O_3:Eu film grown on (100) silicon at 400 °C at 2×10^{-5} Torr.

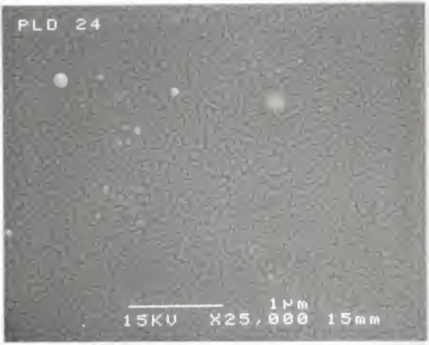

Figure 4-25. SEM photograph of Y_2O_3:Eu film deposited on (100) silicon at 600 °C at 2×10^{-5} Torr.

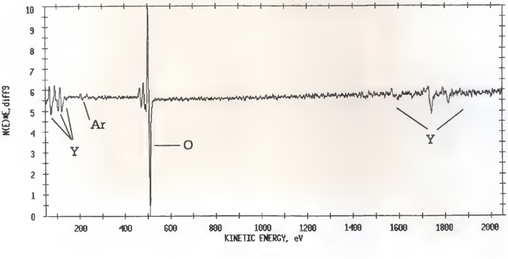

Figure 4-26. Auger electron spectrum from Y_2O_3:Eu thin film deposited on (100) silicon at 600 °C and 200 mTorr, showing the characteristic low energy yttrium triplet (75, 106, 122 eV), oxygen (509 eV), and the high energy yttrium peaks (1743, 1817 eV). The small peak at 215 eV was present from implantation of argon during sputtering.

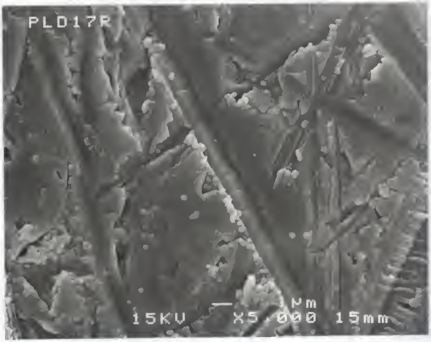

Figure 4-27. SEM photograph of a film grown on (100) silicon at 600 °C and 2 x 10^{-5} Torr on a mechanically roughened substrate with 600 grit SiC paper.

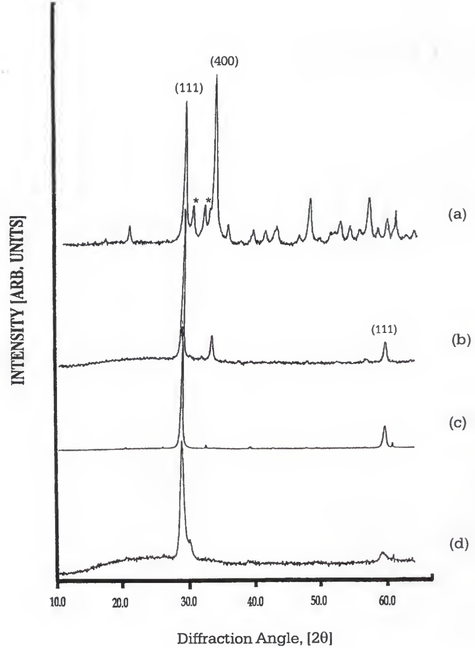

Figure 4-28. X-ray diffraction patterns of Y_2O_3:Eu grown on (100) silicon at 600 °C at oxygen partial pressures of (a) 600 mTorr, (b) 400 mTorr, (c) 200 mTorr, and (d) 0.02 mTorr. Increasing O_2 pressure increased the RMS roughness of the films. Yttrium silicate phase denoted by (*).

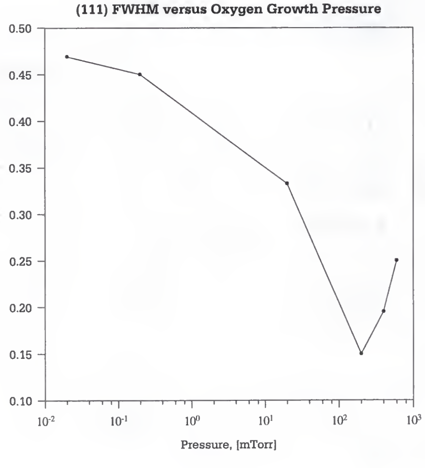

Figure 4-29. Change in FWHM of (111) peak for films grown on (100) silicon at 600 °C at 0.02 mTorr, 0.2 mTorr, 20 mTorr, 200 mTorr, 400 mTorr and 600 mTorr of oxygen growth pressure.

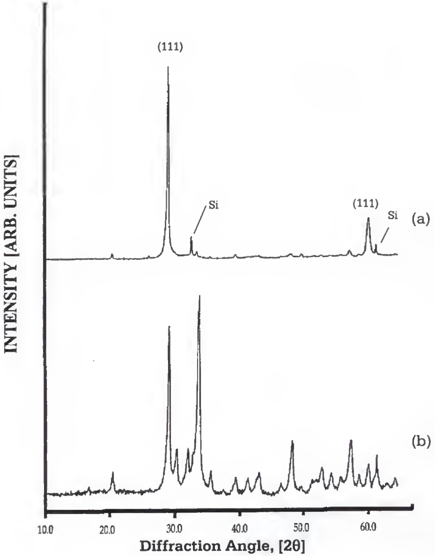

Figure 4-30. X-ray diffraction patterns showing the elimination of yttrium silicate phase for a film grown at (a) 200 mTorr for 2 minutes and 11 minutes at 6 Torr versus (b) a film grown at 600 mTorr for 15 minutes. Silicon substrate temperature was 600 °C.

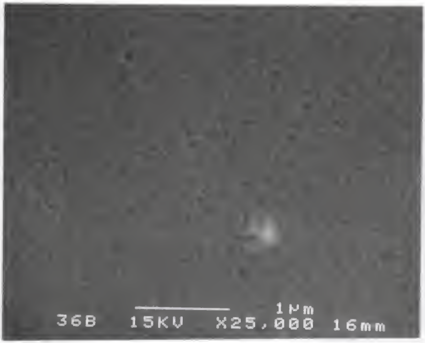

Figure 4-31. SEM photograph of film grown at 0.2 mTorr on (100) silicon and 600 °C showing a smooth surface.

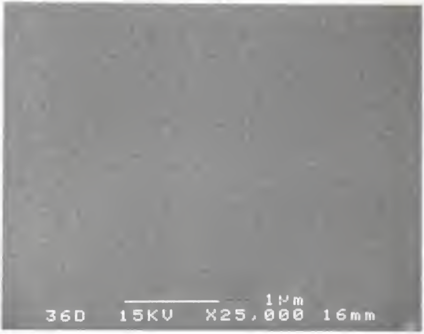

Figure 4-32. SEM photograph of film grown on (100) silicon at 20 mTorr and 600 °C showing a smooth surface.

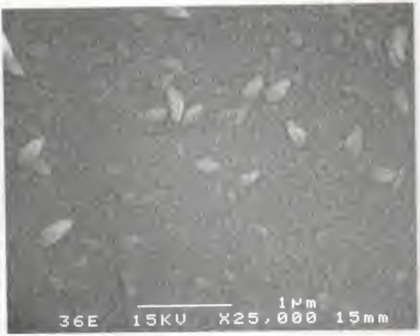

Figure 4-33. SEM photograph of film grown on (100) silicon at 200 mTorr and 600 °C showing outgrowths and the on-set of surface roughness. The estimated RMS roughness was 10 nm.

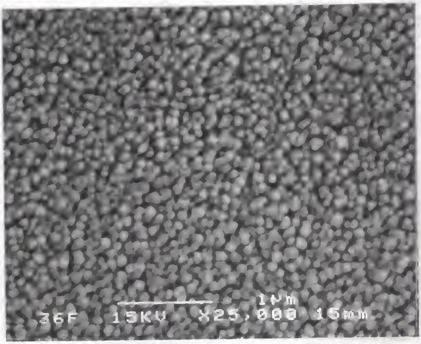

Figure 4-34. SEM photograph of film grown on (100) silicon at 400 mTorr and 600 °C showing a nodular surface with a RMS roughness of 20 nm.

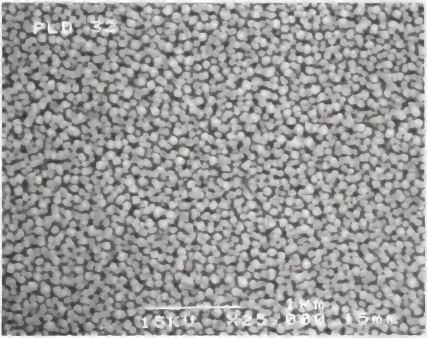

Figure 4-35. SEM photograph of film grown on (100) silicon at 600 mTorr and 600 °C showing a nodular surface with a RMS roughness of 71 nm.

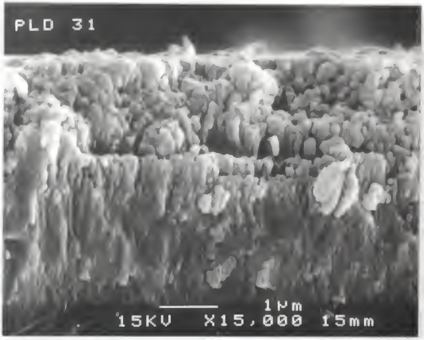

Figure 4-37. SEM photograph illustrating in-situ change in morphology and microstructure with increasing growth pressure. Film grown on (100) silicon at 600 °C at 0.05 mTorr to 80 mTorr, 600 mTorr, and then 1 Torr.

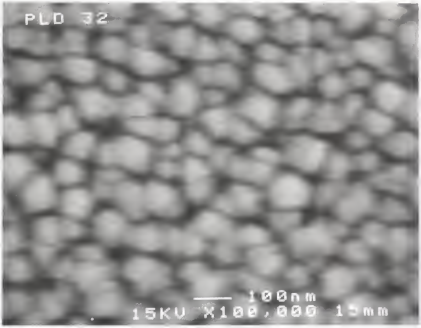

Figure 4-36. SEM (100,000x) photograph showing nanoparticle features of film grown at 600 mTorr and 600 °C on (100) silicon.

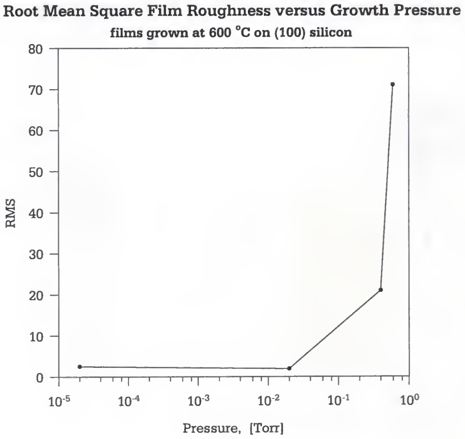

Figure 4-38. Plot of RMS versus increasing O_2 growth pressures. Silicon substrate temperature was 600 °C for all depositions.

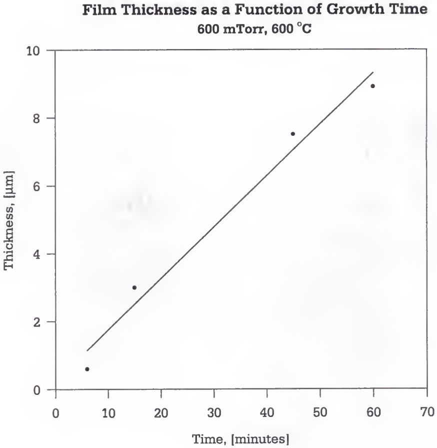

Figure 4-39. Film thickness versus growth time for 600 °C substrate temperature and 600 mTorr of O_2 pressure. Plot shows linear increase in film thickness as growth time is increased.

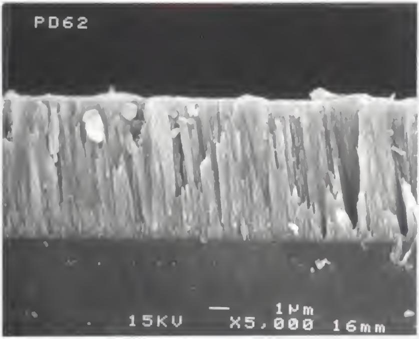

Figure 4-40. Cross-section SEM photograph of film grown on (100) silicon at 600 mTorr and 600 °C for 60 minutes.

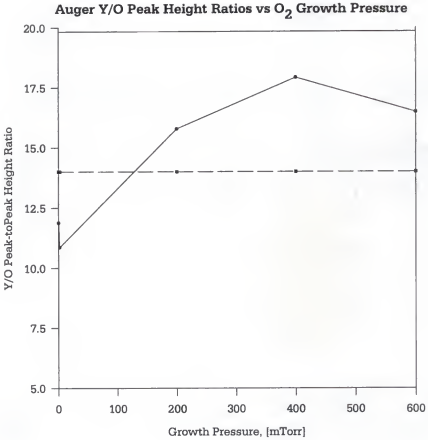

Figure 4-41. Auger Y/O peak height ratios for different oxygen growth pressures. The target (dotted line) had a Y/O ratio of 14.

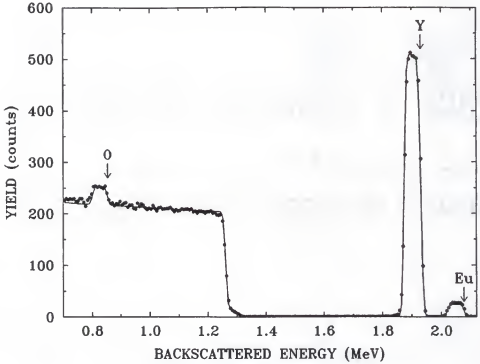

Figure 4-42. Rutherford Backscattering spectrum of film grown on (100) silicon at 100 mTorr O_2 pressure and 600 °C for 1 minute.

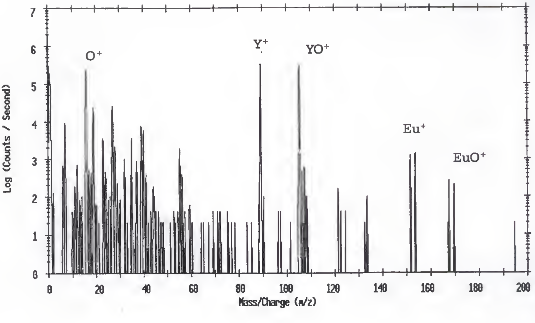

Figure 4-43. SIMS surface scan of film grown on (100) silicon at 600 °C and 600 mTorr, showing surface contaminants, oxygen at a mass/charge ratio of 16, yttrium at 89 and europium at 151 and 153.

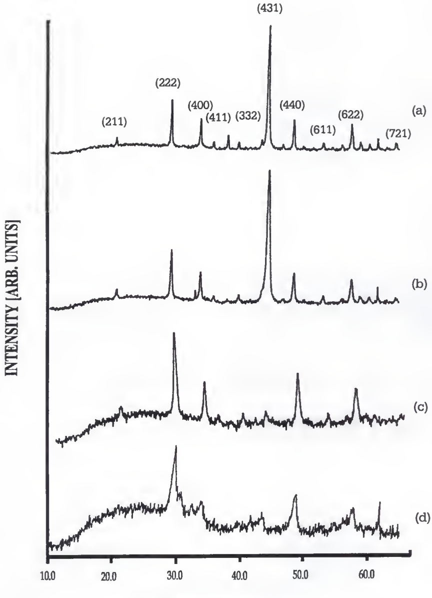

Figure 4-44. X-ray diffraction patterns showing the effect of annealling temperature on yttria films deposited on (100) silicon in 600 mTorr O_2 pressure at 460 °C followed by annealing at (a)1200 °C, (b) 1000 °C, (c) 800 °C, and (d) as-deposited. Films were furnaced annealed in air for 60 minutes.

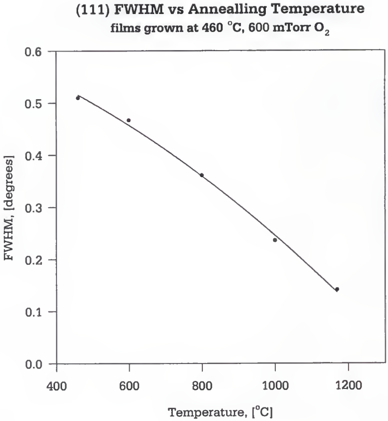

Figure 4-45. FWHM versus annealing temperature for films grown on (100) silicon at 460 °C and 600 mTorr and annealed in air for 1 hour at varous temperatures showing a decrease in FWHM as the temperature is increased.

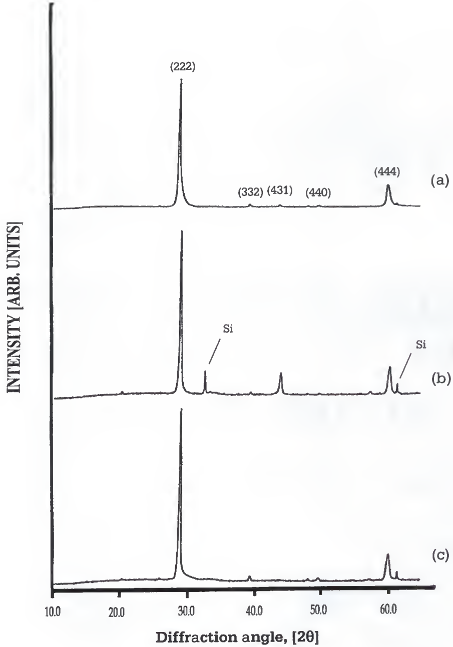

Figure 4-46. X-ray diffraction patterns showing the effect of annealing temperature on yttria films grown on (100) silicon at 100 mTorr and 450 °C furnaced annealed in air at (a) 1200 °C, (b) 1000 °C, and (c) 800 °C for 1 hour.

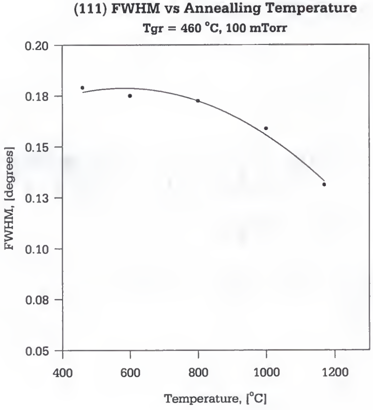

Figure 4-47. FWHM versus annealing temperature for films grown on (100) silicon at 460 °C and 100 mTorr and annealed in air for 1 hour at various temperatures.

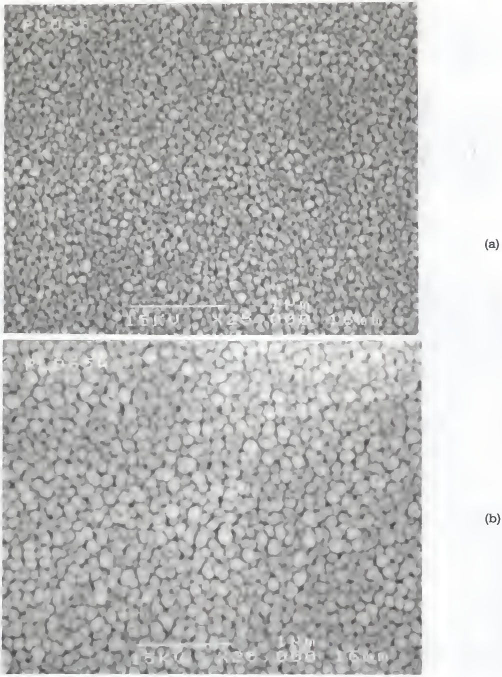

Figure 4-48. SEM photograph comparing (a) as-deposited film (600 mTorr, 600 °C) versus (b) a film annealed at 1000 °C for 30 minutes.

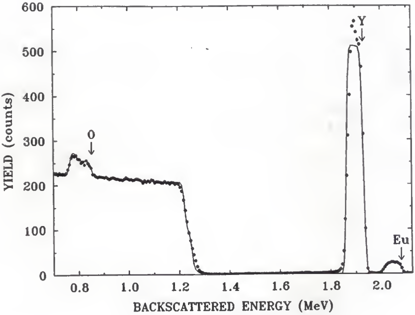

Figure 4-49. RBS spectrum of film annealed at 1000 °C for 30 minutes showing Si, O, Y, and Eu peaks. Also shows a reaction at the Si interface with O, Si, and Y. Solid line represents fit of data to determine composition.

CHAPTER 5

DISCUSSION

The primary intent of this work was to determine the effects of changing surface morphology on the PL and CL brightness of Y_2O_3:Eu thin films grown on silicon. The data show that in-situ changes in surface morphology at high O_2 pressure during PLD resulted in enhanced luminescence. This was attributed to light scattering effects that reduced the light piping. This is further discussed below in terms of optical scattering theory. The effects of film growth temperature, pressure and annealing on PL and CL brightness are also discussed.

Enhanced Luminescence Through Scattering

Increasing the RMS roughness through increased growth pressures above 200 mTorr resulted in increased luminescent brightness detailed by the optical spectrometer. This was attributed to forward scattering of light at the film/air interface being increased while internal reflectance was decreased at higher roughness. The reported values for RMS roughness were between 3 to 71 nm and the grain sizes were approximately 80 nm.

A model of surface scattering assumes that the grains and surface particles are uniform and that the surface looks similar to figure 5-1, where a is the RMS roughness, b is the surface hillock (grain) size and c is the spacing between particles. It is assumed that the RMS roughness is the proper roughness term to model the parameter a and that c is large enough that the surface particles do not act as closely packed particles but as individual scatters. It was also assumed that the film had the bulk index of refraction value for yttria at 611 nm (n=1.93) and that due to the columnar structure of the films, the light impinges as a plane wave incident parallel to the scattering surface.

From the previous discussion on scattering (chapter 2), it was shown that scattering theory, as opposed to geomtric optics, was appropriate for small particles with index of refraction close to 1. From the size parameters, x, and ρ, the critical dimensions at the largest RMS are equal to

$$x = \frac{2\pi a}{\lambda} = 0.73 \quad ; \quad \rho = 2x|m-1| = 1.36$$

where the sample RMS roughness substitutes for a. These values are too high to satisfy the conditions for Rayleigh scattering ($a < \lambda/20$ and $1.93x<1$). Although Rayleigh-Gans scattering allows for a larger x value, both x and ρ are still too small ($(m-1)x << 1$). Even the limiting case of Rayleigh-Gans, intermediate scattering, is excluded since the ρ value is greater than 1.

Since the RMS roughness was not greater than λ, geometric optic ray tracing is not valid. Anomalous diffraction is appropriate, however, since x is larger than $\lambda/20$ and ρ is greater than 1. The scattering efficiency, Q_{sca}, is therefore equal to

$$Q_{sca} = 2 - \frac{4}{\rho}\sin\rho + \frac{4}{\rho^2}(1-\cos\rho)$$

The anomalous diffraction scattering efficiency for the yttria system versus ρ and RMS roughness is shown in figure 5-2. It can be seen that as the RMS roughness is increased, the scattering efficiency increases and passes through a maximum of 3.17 at 214 nm. Figure 5-3 shows the same curve magnified for RMS roughness values up to 250 nm. As seen from figure 5-4, the PL response from films grown on (100) silicon at 600 °C show the same sine integral increase as seen in figure 5-3. Using the scattering efficiency, the predicted PL brightness versus RMS roughnesses is shown in figure 5-5. The figure shows that anomalous diffraction theory gives a good fit for surface scattering. So, according to figures 5-2 and 5-3, the PL brightness can be improved significantly with further increases in RMS roughness to values of 214 nm.

This anomalous diffraction also increased the CL efficiency as seen n figures 5-6 and 4-12. Although anneals at temperatures greater than 800 °C were required, the rougher films had brightnesses 3x the smooth films just as in PL. The rough film CL efficiency was still lower than the target and the powder (figure 5-7). Possible reasons for this deviation are given below.

CIE and Reduced Luminescence

The Commission Internationale d'Eclairage (CIE) chromaticity coordinates (x,y) were recorded during CL measurements to characterize the color from the phosphors. The 1931 CIE diagram shown in figure 5-8 shows the (x,y) chromaticity values that correspond to the different primary wavelengths of blue, green and red at 400, 520, and 700 nm, respectively.[Wys78] The (x,y) chromaticity values for a phosphor are functions of the spectral distribution and define the color a phosphor emits.

Phosphors doped with europium may emit in the red (611 to 626 nm), but can have chromaticity or color from whitish- orange to a deep red dependent on the europium concentration.[Bla74, Oza90] As shown in figure 5-9, as the europium mole percent is increased, there is an increase in the x-chromaticity value and a decrease in the y-chromaticity value which corresponds to a shift to deep red, which is also seen in figure 5-8.[Oza90] This shift results from changes in the ratio of from $^5D_1$ - $^7F_1$ and ^5D_o - $^7F_2$ emission peaks at 538 and 611 nm, respectively (figure 5-9). As the concentration of europium active in C_2 sites increases, the ratio decreases and there is a shift towards higher x-chromaticity and lower y-chromaticity values.[Oza71,Oza90]

The increase in europium concentration also has a direct effect on the CL efficiency.[Oza68,Oza90] As the europium concentration is increased, the efficiency increases until there are so many activators that concentration quenching is observed. As shown in figure 5-10, the optimum concentration for Y_2O_3:Eu is 3 mole percent and according to figure 5-9, the (x,y) chromaticity coordinates for this concentration are (0.64,0.35).

The Osram Sylvania powder had CIE chromaticity (x,y) values of (0.644, 0.35) at 2 kV. As seen in figure 5-11, the (x,y) coordinates for the powder changed as a function of voltage below 2 kV. The most probable explanation for this behavior is that above 2 kV, the electron penetration depth was large enough to reach the average 3 mole % europium concentration below the surface, resulting in the x,y coordinates of 0.64, 0.35. Below 2 kV, penetration was shallow and the low x, high y suggests that the europium is depleted from the surface. Figure 5-12 shows the change in x for the powder standard, ablation target and a typical annealed film versus the electron voltage. Note that the thin film phosphor's x-coordinate value is significantly lower, leading to a lower efficiency since the (x,y) coordinate and the efficiency are directly proportional to the activator concentration.[Oza68, Oza90] The films grown from 0.02 mTorr to 600 mTorr had x values that ranged from 0.609 to 0.62 and had an orange-red color associated with them under CL again suggesting Eu depletion. According to figure 5-9, the active Eu concentration in the thin films was about between 2.25 to 2.5 mole percent. This percentage should be increased so an accurate comparison of efficiency between the powder and thin films can be made.[Oza90] This lower europium concentration, evident from lower x-chromaticity values, contributes to a lower CL efficiency from these PLD thin films.

Since the target x,y values closely matched the powder, the europium depletion in the film was a result of the PLD growth process. The RBS data showed that the atomic formula was $Y_{0.367}Eu_{0.007}O_{0.626}$ which corresponds to $Y_{1.835}Eu_{0.035}O_{3.13}$. Using 3 mole percent of europium as the target amount, the molecular formula should have been $Y_{1.85}Eu_{0.15}O_3$. The europium concentration was half that, suggesting that the percentage is as low as 1 to 1.5 mole percent. It is possible that the plume distance from the target was large enough that heavy atoms were not incorporated ideally but were resident in the fringes of the plume. Europium has atomic mass of 153, while yttrium is 89. It is known from spectroscopy experiments on laser ablation plumes that heavier atoms and clusters "fall out" from the plume where the concentration decreases from the center to the outer edge of the plume by a cosine law dependence.

Thin Film Growth

Deposition of Y_2O_3:Eu thin films as reported above yielded crystalline as-deposited thin films at temperatures of 250 °C and higher. As expected, the full width at half maximum (FWHM) for the (111) XRD peak decreased as the substrate temperature was increased, indicating an improvement in crystallinity (figure 4-17). Similar results for FWHM were seen for films deposited onto glass and c-axis Al_2O_3.

Based on data in figures 4-18 and 4-19, films deposited at 250 °C, $< 10^{-4}$ Torr, exhibited slight polycrystalline behavior on crystalline substrates. Between growth temperatures of 250 °C and 800 °C, the films exhibited strong preferential (111) orientation. Above 800 °C, strong polycrystalline texture was developed. This tendency toward strong (111) texturing at temperatures of 800 °C and below has also been reported with PLD of Y_2O_3 by Hirofumi et al.[Hir89] Textured films have also been reported with other growth techniques such as sputtering [Ait93], evaporation [Hud95] and by sol gel [Rao96]. Rao et al. also reported the change to polycrystalline texture at growth temperatures of 800 °C or more.

Films grown at low pressures (2×10^{-5} Torr) were fairly smooth (figure 4-24) while cracked films were observed at growth temperatures of 600 °C or greater (figure 4-25). This most likely resulted from cooling the substrate too rapidly after growth, where the thermal expansion mismatch induced cracking. Silicon has a linear coefficient of thermal expansion(CTE) of 2.49×10^{-6} K^{-1} at 300 °K [Lid97] while yttria has a CTE value of 8.9×10^{-6} K^{-1} [Tro95], which is 3.6 times that of silicon. Columnar growth was also seen (figure 4-22, 4-37 and 4-40) as expected. Growth from high energetic thin film growth processes like PLD and sputtering frequently produce this type of microstructure.[Smi95]

As the oxygen pressure was increased from 0.02 mTorr, the film quality improved. The decrease in (111) FWHM peak (figure 4-29) showed an improvent in crystallinty, with a minimum of 0.15 degrees at 200 mTorr. However, further increases in growth pressure increased the FWHM. This also corresponded to the end of (111) preferential orientation and the onset of polycrystalline behavior (figure 4-28). The AES Y/O peak-to-peak height ratios show that the stoichiometry approached the best ratio between 100 to 200 mTorr, which correlates with the minimum (111) FWHM XRD data quite nicely. This was expected since PLD is usually carried out in the presence of either a reactive gas (O_2, N_2, H_2) or an inert gas (Ar) in the range of a few hundred mTorr to influence stoichiometry.[Hor94] The background gas influences film growth by reducing the energy of the vapor flux impinging the substrate and providing a high flux of gas particles bombarding the surface during deposition. For PLD of oxides in particular, it has been shown that growth pressures between 100 to 300 mTorr are standard in achieving proper stoichiometry and the best bulk film properties.[Pin92]

There was also a change in the surface as the background gas was increased which was expected. In a background pressure of 200 mTorr, outgrowths resulted in a rough surface. Above 200 mTorr, modest improvements in roughness were obtained, and the largest roughness was found at 600 mTorr. As seen in figure 4-38, the root mean square roughness (RMS) was approximately 2 nm for low O_2 pressures, but increased to 71 nm at 600 mTorr. Previous work has shown that pulsed laser ablation can be used for film growth (UHV to 300 mTorr) or to generate particulates (1 Torr to 760 Torr).[Mat86]

The ultimate goal of increasing the brightness by surface modification was achieved. Here, it has been shown that films can be fabricated in-situ with a particle like texture,which improves the efficiency. Surface modification has previously been accomplished by changing the repetition rate [Cha90] or by post deposition laser processing [Fol94]. This is, however, the first report of intentionally utilizing the growth pressure to effect the surface morphology. As noted by Chen [Che94b], the use of reactive or inert gases during growth has not been fully explored beyond the extremes of achieving stoichiometry or producing small sized powder particles. Only recently has it been explored as a technique to fabricate composites and nanophases.[Che94b]

Annealing

Annealing improved the crystallinity of the films. However, the (111) FWHM from annealed films (minimum of 0.14°) were not as low as the value of the powder (0.09° to 0.11°). Annealing at high temperatures should have improved the FWHM. However, the melting temperature of yttria is 2683 °K, so annealing at 1443 °K only yields $0.54*T_{melt}$. The temperature ratio (T_s/T_{melt}) of 0.54 is low in the zone for grain growth (figure 5-13). As seen in the SEM photos of figure 4-48, an annealed film at 1273 °K ($0.47*T_{melt}$) did not show significant grain growth or increase in particle size.

Throughout the annealing process, the smooth film's FWHM remained the lowest. This suggest that crystallinity was better for smooth versus rough polycrystalline films. The brightness and efficiency, however, of smooth films were significantly lower than rough films grown at 600 mTorr (figures 5-6, 5-14 and 5-15).

The effect of improved crystallinity versus increased dopant activation was shown with CL efficiency versus temperature and (111) FWHM (figures 5-14 and 5-15). As seen in the figures, there was a significant increase in efficiency with increasing temperature and a corresponding decrease in FWHM. However, from the activation energy plots (figures 5-16 and 5-17) the reverse was possibly true. The activation energies as a function of annealing temperature were approximately equal, 26 cal/mole for a smooth versus 28 cal/mole for rough films. The activation energies as a function of FWHM, however, show no correlation at all, where E_a is equal to 107 cal/mole for smooth versus 33 cal/mole for rough films. This implies that although there was a significant reduction in FWHM, it was the activation of the europium that was responsible for such an increase in efficiency with annealing temperature. This was also seen in a change in CIE values as the temperature was increased from 1000 °C to 1200 °C, where the x changed from 0.611 to 0.625 and y from 0.364 to 0.359, respectively at 4 kV and 1 $\mu A/cm^2$. This shows an increase in acitve europium.

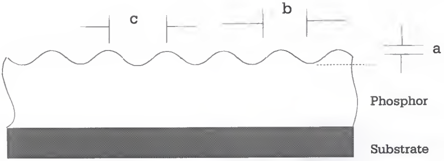

Figure 5-1. Illustration of critical dimensions for roughness of thin film scat terer, where a is the root mean square (RMS) roughness, b is the grain size, and c is the spacing between features.

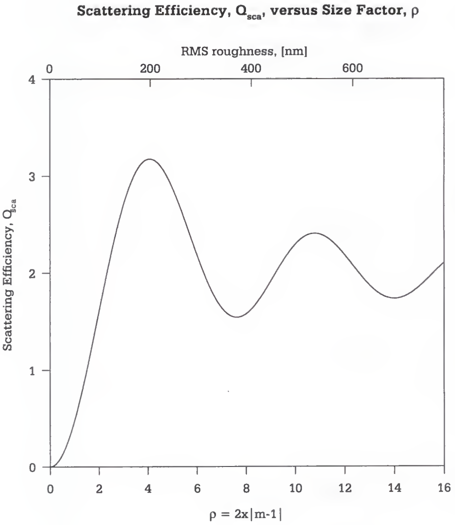

Figure 5-2. Scattering efficiency factor, Q_{sca}, versus the size factor, ρ showing the increase in scattering as the critical dimension, RMS roughness, is increased.[Van81]

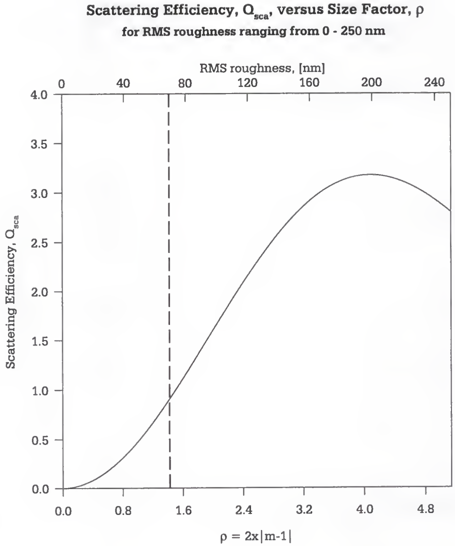

Figure 5-3. Magnification of figure 5-2 for RMS roughness values between 0 and 250 nm showing the scattering efficiency factor, Q_{sca}, versus the size factor, ρ, and RMS roughness. Plot shows the increase in scattering as the critical dimension, RMS roughness, is increased. [Van81] Dotted line represents the maximum RMS roughness obtained in this study in relation to the maximum attainable brightness.

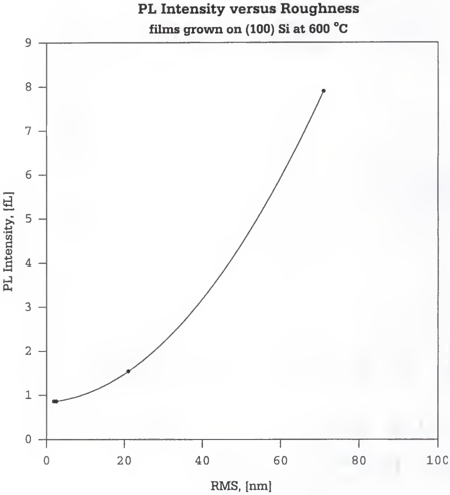

Figure 5-4. Photoluminescence intensity versus root mean square roughness (RMS) for films deposited at various growth pressures on (100) silicon at 600 °C.

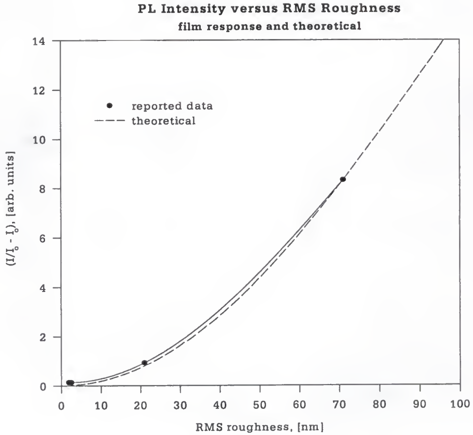

Figure 5-5. Photoluminescence intensity versus RMS roughness of experimental values and theoretical according to anomalous diffraction, as seen in figures 5-2 and 5-3. Plot shows that reported brightness increases due to scattering from surface roughness fits anomalous diffraction theory well.

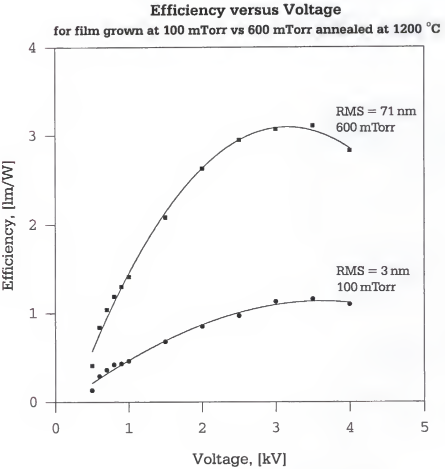

Figure 5-6. Efficiency of 3 μm thick smooth (100 mTorr) versus rough film (600 mTorr) taken at 1 $\mu A/cm^2$ at varying voltages. Films grown on (100) silicon at 460 °C and annealed at 1200 °C in air for 60 minutes.

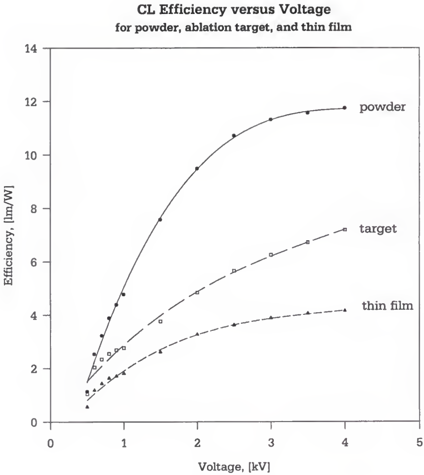

Figure 5-7. Cathodoluminescence efficiency versus voltage taken at 1 μA/cm^2 of standard, ablation target, and 9 μm thick rough film. Target was sintered at 1400 °C for 24 hours. Thin film was deposited on (100) silicon at 600 °C, 600 mTorr and annealed at 1200 °C in air for 60 minutes.

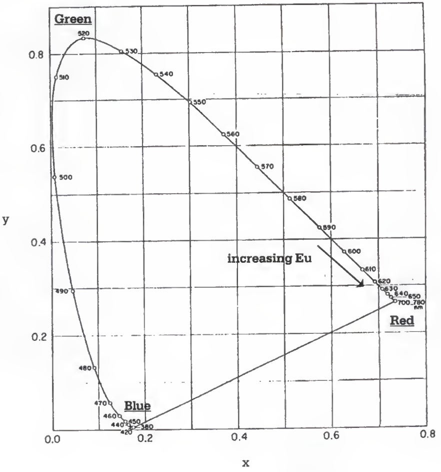

Figure 5-8. The 1931 Commission Internationale de l'Eclairage (CIE) (x,y) chromaticity diagram showing the three primary color regions blue, green and red as a function of chromaticity values x and y. [Wys78] The arrow shows the change in (x,y) as europium concentration is increased.

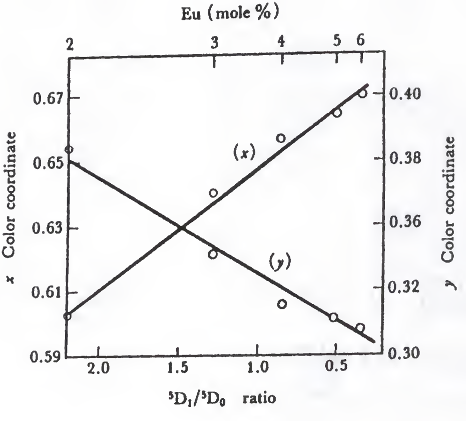

Figure 5-9. Plot of x and y chromaticity values versus europium mole percent and europium S_6/C_2 site emission for Y_2O_2S under cathode ray excitation.[Oza90]

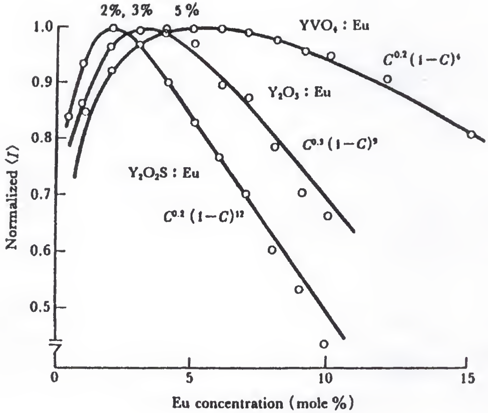

Figure 5-10. Plot of luminescence intensity versus europium concentration for Y_2O_2S, Y_2O_3 and YVO_4 phosphors showing the optimum europium concentration for each phosphor system. Concentration quenching occurs at mole percents greater than this critical value. For Y_2O_3, this value is 3 mole percent.[Oza90]

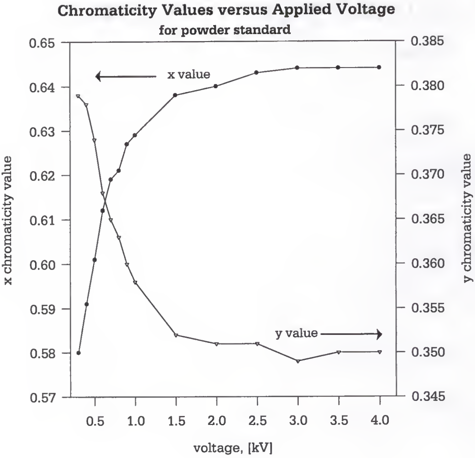

Figure 5-11. Change in x and y chromaticity values for powder standard as a function of applied voltage, where the x value increases to 0.644 and the y value decreases to 0.350 as the voltage is increased.

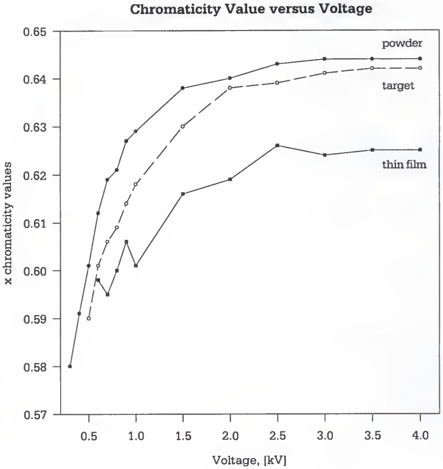

Figure 5-12. Change in x chromaticity value for powder standard versus film grown at 460 °C, 600 mTorr and annealed 1 hour in air at 1200 °C showing that the films x-value is 0.625 instead of 0.644 (powder) or 0.639 as in the case of the target.

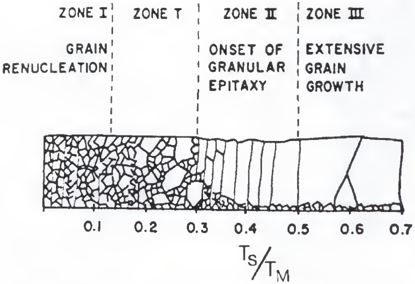

Figure 5-13. Zone model of grain size changes for metals deposited at substrate temperature, T_s versus their melting temperature, T_{melt}. Temperature is in Kelvin.[Ohr92]

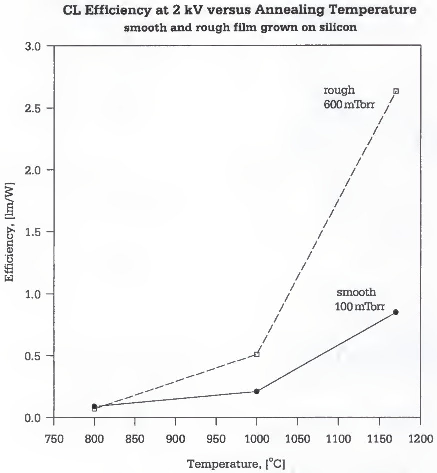

Figure 5-14. Cathodoluminescence efficiency versus annealing temperature for a smooth film (100 mTorr) and rough film (600 mTorr) showing the increase in the efficiency with annealing temperature. Films were deposited on (100) silicon at 460 °C and annealed at various temperatures for 60 minutes in air.

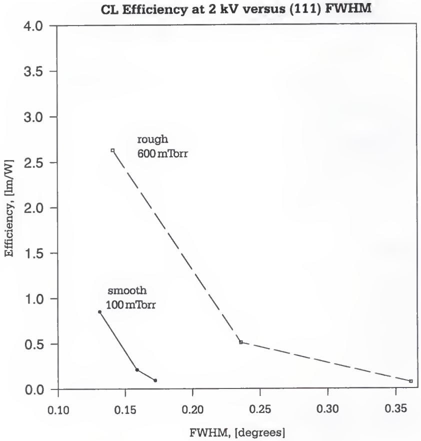

Figure 5-15. Cathodoluminescence efficiency versus FWHM for a smotth film (100 mTorr) and a rough film (600 mTorr) showing the increase in the efficiency for increased crystallinity. Films were deposited on (100) silicon at 460 °C and annealed at various temperatures for 60 minutes in air.

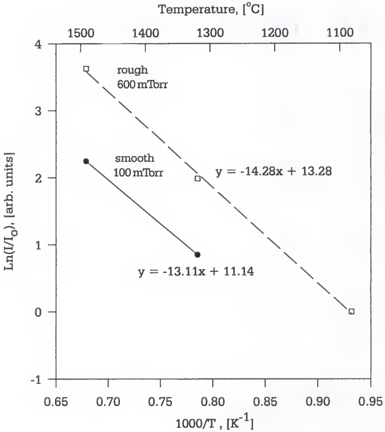

Figure 5-16. Plot of activation energy for change in CL efficiency versus annealing temperature showing similar activation energies for films grown on (100) silicon at 460 °C and annealed at various temperatures for 1 hour in air. The smooth film (100 mTorr) has an activation energy, E_a, equal to 26 cal/mole while the rough film (600 mTorr) has an E_a equal to 28 cal/mole.

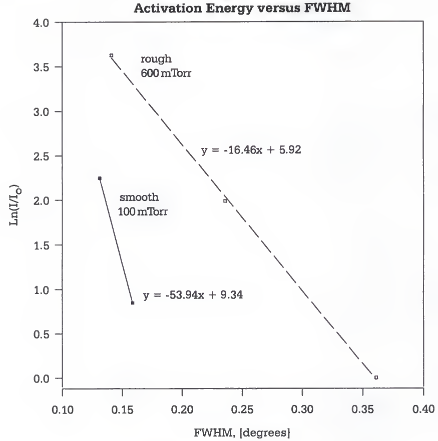

Figure 5-17. Plot of activation energy for change in FWHM showing dissimilar activation energies for films grown on (100) silicon at 460 °C and annealed at various temperatures for 60 minutes in air. The smooth film (100 mTorr) has an activation energy, E_a, equal to 107 cal/mole while the rough film (600 mTorr) has an E_a equal to 33 cal/mole.

CHAPTER 6

SUMMARY AND CONCLUSIONS

Yttrium oxide doped with 4.5 weight percent europium films were deposited onto (100) silicon, glass, and c-axis Al_2O_3 substrates using pulsed laser ablation (PLD). The luminescence versus deposition conditions and microstructure were characterized and correlated. The PLD target demonstrated cathodoluminescence (CL) and photoluminescence (PL) efficiencies and brightnesses a factor of 2 lower than the Y_2O_3:Eu starting powder phosphor while the thin films were a factor 3.3 lower. This correlated to an increase in theoretical and experimental values of 7% outcoupling for smooth films to 30% from rough films.

As-deposited films were crystalline at substrate temperatures as low as 250 °C, even though the melting temperature of Y_2O_3 is 2410 °C. The PLD films had particules varying in size from 100 ± 15 nm to 80 ± 15 nm for pressures of 2×10^{-5} Torr to O_2 pressures of 600 mTorr, respectively. PLD at temperatures less than 600 °C and oxygen pressures below 200 mTorr resulted in preferentially oriented films with a (111) texture. An increase in the O_2 pressure above 200 mTorr and growth temperature above 600 °C changed the film from (111) texture to a random polycrystalline orientation. For O_2

pressures between 2 x10^{-5} Torr and 200 mTorr, the (111) FWHM decreased from 0.47 to 0.15, then increased to 0.25 degrees at 600 mTorr. However, the PL and CL intensities increased dramatically up to 600 mTorr of O_2 with little improvement at higher oxygen pressures. The grain and particulate size was also reduced as the pressure was increased. Since the average particle size of the Y_2O_3:Eu PLD thin films was less than 200 nm, there is hope that films with sub-micron or even nanosized grains can be efficient emitters. Phosphor powders less than 1 μm are significantly less efficient than powders optimized for CRT applications having particle sizes ranging from 3 to 10 μm. At processing conditions of $T \geq 600$ °C and $P_{O2} \geq 600$ mTorr, α-$Y_2Si_2O_7$ was formed at the Y_2O_3/silicon interface.

The reported increased PL brightness with increased oxygen pressure resulted from an altered surface morphology. The RMS surface roughness increased from 2 nm to 71 nm upon increasing the growth pressure from 200 mTorr to 600 mTorr, with a concomitant increase in PL brightness from 0.162 fL to 0.833 fL for 1 μm thick films, respectively. However, brightness was only 1.5% and 7.9% that of a powder standard for a smooth film and rough film, respectively. Increasing film thickness to 3 μm and 9 μm increased the brightness to 2.5 fL (22.7%) and 3.9 fL (35.6%), respectively for rough films deposited at 600 mTorr and 600 °C.

The increase in RMS lead to increased forward diffuse scattering which was fitted to anomalous diffraction scattering equation of the sine integral form

$$Q_{sca} = 2 - \frac{4}{\rho}\sin\rho + \frac{4}{\rho^2}(1 - \cos\rho).$$

Using this theory, it was predicted that the maximum gain in efficiency from this type of scattering would be at RMS roughness values close to 200 nm. This roughness was well beyond the in-situ capabilities of PLD.

Annealing samples grown at 460 °C in various oxygen pressures to temperatures between 600 °C and 1200 °C increased the CL brightness and efficiency. As the annealing temperature increased, the brightness and efficiency increased and the (111) FWHM decreased. For smooth films deposited at 100 mTorr and 400 °C, the (111) FWHM decreased from 0.18° to 0.13° degrees after annealing at 1170 °C in air for 1 hour. Rough films grown at 600 mTorr and 400 °C decreased in (111) FWHM from 0.51 to 0.14 degrees upon the same annealing schedule. The smooth films retained the (111) texture, while rough films changed to more random polycrystalline orientations. Again, α-yttrium silicate phase formed at the Y_2O_3/Si interface. After the 1170 °C anneal, the smooth films had a PL brightness of 1.8 fL while rough films had 4.6 fL. Although the FWHMs were equal for smooth and rough films, the 70 nm RMS roughness film was 2.5 times more efficient in CL. The CL efficiency at 2 kV and 1 μA/cm^2 was 0.85 lm/W (9% of the powder efficiency) and 2.63 lm/W

(28% of powder) for smooth and rough films, respectively. The CL efficiency for a 9 μm thick film at 2 kV and 1 μA/cm^2 was 3.3 lm/W (35 % of powder).

All of the films had CIE x and y coordinates which were lower and higher, respectively, as compared to the powder. The powder had (x, y) values equal to (0.644, 0.352) at 4 kV and 1 μA/cm^2. The films varied with x: 0.601 to 0.625 and y: 0.359 to 0.362. This indicated that the amount of active europium was at least a half of a mole percent less than that of the powder, resulting in much lower efficiency. RBS confirmed that the europium concentration was lower than 3 mole percent.

From the data presented, it is seen that increasing the europium concentration and increasing the scattering efficiency by increasing RMS roughness, the thin film phosphor efficiency could be advanced significantly. These advances could lead to an efficient thin film phosphor system, even at lower processing temperatures. This would provide the FED industry with a high resolution display that is physically and thermally rugged.

CHAPTER 7

FUTURE WORK

This research suggest that light piping effects in thin films can be significantly reduced or even eliminated through surface modifications. Even though the efficiency of the films was improved by increasing the roughness, the brightness was still much lower than the unprocessed, unscreened powder. To utilize the benefits of the higher resolution possible from thin film screens (50 times higher resolution), future work should be done in the categories of optimizing the RMS roughness, optimizing the dopant concentration, improving the as-deposited film crystallinity, and doing experiments to understand and quantify the surface recombination effects in Y_2O_3:Eu thin films. A few suggestions are offered below.

The optimum RMS roughness, according to the anomalous diffraction equation, would be ~ 200 nm, suggesting that the roughness could be further optimized. Roughnesses around this value should be tried, possibly using template substrates manufactured utilizing photolithography techniques. An increase in RMS from 71 nm to 200 nm, theoretically, would triple the efficiency (Q_{sca} from 0.83 to 3.17). The CL efficiency at 2 kV and 1 $\mu A/cm^2$ for the 9 μm thick film would have been 12.66 lm/W, whereas the powder was 9.5 lm/W.

Roughnesses greater than 2λ should also be tried where geometric optics apply. Recent advances in GaAs (n=3.5) LEDs have been achieved by utilizing ray optics to increase the efficiency.[Pea97] The size should be kept close to 1.1 μm so that the particle size advantage over powder phosphors is retained.

Since the CIE versus voltage experiments showed that the europium concentration was much lower than the concentration of the starting powder, a true comparison of efficiency was not possible. Therefore, the europium concentration should be increased to bring the (x,y) coordinates to their proper value and improve the efficiency of the Y_2O_3:Eu films. This could be accomplished by adding $EuCl_3$, EuF_3, or Eu_2O_3 to the starting targets at various weight percents. The chlorine or fluorine addition would also act as fluxing agents that would aid in sintering.

More dopant could also be added by depositing a europium thin film on top of the existing films followed by drive-in anneals to diffuse, homogenize and activate the europium. It would also be worth trying ion implanting europium to the desired concentration followed by annealling to activate the europium and repair the lattice damage done during implantation.

It was also evident that temperature, especially annealing temperature, played a significant role in improving the CL efficiency. The maximum annealing temperature used in this study was 1443 °K, which corresponds to only $0.54*T_{melt}$ of yttria. Such high temperature anneals are not an acceptable option for most flat panel display manufacturers. The development of lower melting temperature phosphors, the incorporation of fluxes to lower the growth temperature, growth schemes utilizing glass formers, or utilizing rapid thermal processing (lasers annealing, rapid thermally annealing) to anneal the film without effecting the substrate should be investigated.

Finally, it is curious that the CL efficiency kept increasing with film thicknesses (9 μm) well beyond the primary electron penetration distance (0.5 μm at 2 kV) and the theoretical electron hole pair generation and diffusion distances. Could there be a reduction of the surface recombination velocity as the distance between the substrate and the film surface increases? Is this velocity the limiting factor in determining the electron-to-activator transfer efficiency, η_t? This could be checked by doing PL lifetime measurements on a smooth film, a rough film, the powder, and the target. If the surface recombination is a significant factor, the decay time will be lower for the films versus the powder and target. Comparison between the smooth versus rough film will also show if there is an effect of surface roughness on the SR. Understanding the surface recombination velocity and what it is a function of may be the key to increasing the efficiency not just for thin films but for powder phosphors as well.

APPENDIX A. CALCULATION FOR FRACTION OF LIGHT EMITTED

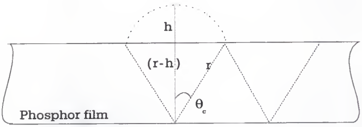

dA/r^2 = solid angle subtended by $2\theta_c$ [Boa83]
$2\theta_c$ = total solid angle
θ_c = half angle = critical angle
$A = 2\pi rh$

$2\theta_c = dA/r^2 = 2\pi rh/r^2 = 2\pi(h/r)$

from the half angle triangle of the emission cone
$\cos(\theta_c) = (r-h)/r = 1 - (h/r)$
$h/r = 1 - \cos\theta_c$

$2\theta_c = 2\pi(1 - \cos\theta_c)$

For a sphere: the total area = 4π, therefore
The percentage emitted over the total area, $f = 2\theta_c/4\pi$

$2\theta_c/4\pi = f = 1/2\,(1 - \cos\theta_c)$

$f = 0.5(1-\cos\theta_c)$

APPENDIX B. ALLOWED (hkl) VALUES FOR X-RAY DIFFRACTION

Bravais lattice	Reflections possibly present	Reflections necessarily absent
Simple	all	none
Base-centered	h and k unmixed*	h and k mixed*
Body-centered	$(h + k + l)$ even	$(h + k + l)$ odd
Face-centered	h, k, and l unmixed	h, k, and l mixed

[Cul78]

REFERENCES

Ald91	Alder, E. A., Bardi, Z., Forman, D. M., Goebel, D. M., Longo, R. To., & Sokolich, M., IEEE Transactions on Electron Devices **38**, 2304.
Ait93	Aita, C. R., Journal of Vacuum Science Technology A **11**, 1540.
Alv72	Alves, R., Buchanan, R., & Maple, T., AGARD Conference Proceedings, 105.
Bat60	Bateman, S. K., Vacuum **10**, 329.
Bau89	Bauerle, D., Applied Physics A **48**, 527.
Bau92a	Bauerle, D., Luk'yanchuk, B., Scwab, P., Wang, X., & Arenholz, E., Laser Ablation of Electronic Materials: Basic Mechanisms and Applications, Elsevier Science Publishers, New York, NY.
Bau92b	Baumann, S.M., Encyclopedia of Materials Characterization, edited by Brundle, C.R., Evans, C. A., & Wilson, S., Manning Publications Co., chapter 9.1.
Bec96	Bechtel, H., Czarnojan, W., Haase, M., Mayr, W., & Nikol, H., Philips Journal of Research **50**, 433.
Bec63	Beckmann, P., & Spizzichino, A., The Scattering of Electromagnetic Waves from Rough Surfaces, The Macmillan Co., New York, NY.
Bhu95	Bhushan, B., editor, Handbook of Micro/Nano Tribology, CRC Press, Boca Raton, FL.
Bin92	Bindell, J.,Encyclopedia of Materials Characterization, edited by Brundle, C.R., Evans, C.A., & Wilson, S., Manning Publications Co., chapter 2.2.
Bin82	Binning, G., Rohrer, H., Gerber, C., & Weibel, E., Physics Review Letters. **49**, 57.

Bla79 Blasse, Chemistry and Physics of R-Activated Phosphors, ed. Gscheindner, K. A. & Eyring, L., Handbook on the Physics and Chemistry of Rare Earths: volume 4, North-Holland Publishing Comp., New York, NY.

Bla94 Blasse, G., & Grabmaier, B.C., Luminescent Materials, Springer-Verlag, Berlin, Germany.

Boa83 Boas, M. L., Mathematical Methods in the Physical Sciences, 2nd Edition, John Wiley and Sons, New York, NY.

Boh96 Bohren, C. F., Handbook of Optics volume I, edited by Bass, M., McGraw-Hill, Inc., New York, NY, chapter 6.

Bon95 Bondar, V., Grytsiv, M., Groodzinsky, A., & Vasyliv, M., SPIE **2648**, 338.

Bor64 Born, M., & Wolf, E., Principles of Optics: Electromagnetic Theory of Propagation, Interference and Diffraction of Light, Pergamon Press, New York, NY.

Bro92 Brodie, I, & Spindt, C. A., Advances in Electronics and Electron Physics volume 83, Academic Press, New York, NY.

Bui87 Buijs, M & Meyerink, A. & Blasse, G., Journal of Luminescence **37**, 9.

Car66 Carr, W. N., Infrared Physics **6**, 1.

Cas92 Castellano, J., Handbook of Display Technology, Academic Press, Inc., San Diego, CA.

Cha90 Chang, C. C. & Wu, X. D. & Ramesh, R. & Xi, X. X. & Ravi, T. S. & Venkatesan, T. & Hwang, D.M. & Muenchausen, R. & Foltyn, S. & Nogar, N. S., Applied Physics Letters **57**, 1814.

Che94a Chen, L., Pulsed Laser Deposition of Thin Films, edited by Crisey, D. & Hubler, G.K., John Wiley and Sons, New York, NY, chapter 6.

Che94b Cheung, J. T., Pulsed Laser Deposition of Thin Films, edited by Crisey, D. & Hubler, G.K., John Wiley and Sons, New York, NY, chapter 1.

Che88 Cheung, J. T., & Sankur, H., CRC Critical Reviews in Solid State and Materials Sciences **15**, 63.

Chu86 Chu, W., Metals Handbook 9th Edition: Vol 10 Materials Characterization, edited by Davis, J., American Society for Metals, Metals Park, Ohio.

Chu78 Chu, W., Mayer, J. W., Nicolet, M., Backscattering Spectrometry, Academic Press, New York, NY.

Chu95 Church, E. L., & Takacs, P. Z., Handbook of Optics volume I, edited by Bass, M., McGraw-Hill, Inc., New York, NY, chapter 7.

Col92 Colvard, C., Encyclopedia of Materials Characterization, edited by Brundle, C.R., Evans, C.A., & Wilson, S., Manning Publications Co., chapter 7.1.

Cul78 Cullity, B.D., Elements of X-ray Diffraction, Addison-Wesley Pub. Co., Reading, MA.

Cus52 Cusano, D.A., & Studer, F.J., Journal of the Optical Society of America **42**, 878.

Cut93 Cutler, P. H., He, J., Mislovsky, N. M., Sullivan, T. E., & Weiss, B., Journal of Vacuum Science and Technology B **11**, 387.

Dal92 Dalacu, N., Kitai, A. H., Sanders, B. W., & Huang, R., Thin Solid Films **209**, 207.

DeJ97 DeJule, R., Semiconductor International **20**, 59.

Die68 Dieke, G. H., Spectra and Energy Levels of Rare Earth Ions in Crystals, International Publishers, New York.

Eye87 Eyett, M. & Bauerle, D., Applied Physics Letters **51**, 2054.

Fal92 Falcony, C., Garcia, M., Ortiz, A., & Alonso, J., C., Journal of Applied Physics **72**, 1525.

Fel60 Feldman, C., Physical Review **117**, 455.

Fel57a Feldman, C., M., Journal of the Optical Society of America **47**, 790.

Fel57b Feldman, C. & O'Hara, M., Journal of the Optical Society of America **47**, 300.

Fol94 Foltyn, S. R., Pulsed Laser Deposition of Thin Films, edited by Crisey, D. & Hubler, G.K., John Wiley and Sons, New York, NY, chapter 4.

For69 Forest, H. & Ban, G., Journal of the Electrochemical Society **116**, 474.

Gav90 Gavigan, J.,Givord, D.,Lienard, A., McGrath, O., Rebouillant, J., & Souche, Y., MRS Symposium Proceedings volume 191.

Gol66 Goldberg, P, Luminescence of Inorganic Solids, edited by Goldberg, P., Academic Press, New York, NY, chapter 7.

Gre94a Green, S., Pique, A., Harsjavardhan, K., & Bernstein, J., Pulsed Laser Deposition of Thin Films, edited by Chrisey, D. & Hubler, G.K., John Wiley and Sons, NY, New York, chapter 2.

Gre94b Greer, J., Van Hook, V. H., Tabat, M., Nguyen, H., Gammie, G., & Koufopoulos, P., MRS Symposium Proceedings volume **345**, 281.

Gro89 Grovernor, C. R. M., Microelectronic Materials, edited by Cantor, B., Institute of Physics Publishing Ltd, Philadelphia, PA.

Gu91 Gu, Z., Dummer, R. S., Maradudin, A. A., McGurn, A. R., & Mendez, E. R., Applied Optics **30**, 4094.

Gui95 Guillaume, C.B.A.L., Encyclopedia of Applied Physics vol 13, edited by Trigg, G.L., VCH Publishers, Inc., NY, New York.

Han65 Hansen, W. W. & Myers, R. E., Applied Physics Letters **6**, 58.

Has90 Hase, T., Kano, T., Nakazawa, E., & Yamamoto, E., Advances in Electronics and Electron Physics vol. 79.

Hen89 Henderson, B., & Imbusch, G.F., Optical Spectroscopy of Inorganic Solids, Oxford University Press, New York, NY.

Hir97 Hirata, G.A., McKittrick, J., Avalos-Borja, M., Siqueiros, J.M., & Devlin, D., Applied Surface Science **113/114**, 509.

Hir96 Hirata, G. A., McKittrick, J., Shea L. E., Avalos-Borja, M., & Lopez, O. A., Applied Surface Science **113/114**, 509.

Hir89 Hirofumi, F., Imura, T., & Osaka, Y., Applied Physics Letters **55**, 360.

Hol80 Holloway, P. H., Advances in Electronics and Electron Physics volume 54, Academic Press, New York, NY.

Hol96 Holloway, P. H., Jones, S.L., Rack, P., Sebastian, J., & Trottier, T., Proc. Of Tenth Intl. Sym. Applications of Ferroelectrics, edited by B. Kulwicki, East Brunswick, NJ, (IEEE, NY).

Hol95 Holloway, P. H., Sebastian, J., Trottier, T., Swart, H. & Peterson, H., Solid State Technology **38**, 47.

Hor94 Horwitz, J. S., & Sprague, J. A., Pulsed Laser Deposition of Thin Films, edited by Chrisey, D. & Hubler, G.K., John Wiley and Sons, New York, NY, chapter 8.

How93 Howland, R., & Benatar, L., A Pratical Guide to Scanning Probe Microscopy, Park Scientific Instruments.

How92 Howland, R. S., & Kirk, M.D., Encyclopedia of Materials Characterization, edited by Brundle, C.R., Evans, C.A., & Wilson, S., Manning Publications Co., chapter 2.3.

Hsi94 Hsieh, I., J., Feng, M., S., Kuo, K. T., & Lin, P., Journal of the Electrochemical Society **141**, 1617.

Hud92 Hudson, J., Surface Science: An Introduction, Butterworth-Heinmann, Boston, MA.

Huo86 Huo, D., & Huo, T., Journal of the Electrochemical Society **133**, 1492.

Ino95 Inoue, Y., Tanaka, K., Okamoto, S., Kobayashi, K., & Fujimato, K., Japanese Journal of Applied Physics **34**, 180.

Jae93 Jaeger, R. C., Introduction to Microelectronic Fabrication: Volume 5, Addison-Wesley Publishing Company, Reading, MA.

Jag94 Jagannathan, R., Kutty, T.R.N., Kottaisamy, M. & Jeyagopal, M., Japanese Journal Applied Physics **33**, 6207.

Jen76 Jenkins, F. A., & White, H. E., Fundamentals of Optics, edited by Fry, R. A., & Vinnicombe, A., T., McGraw-Hill, Incorporated, New York, NY.

Jol90 Jollet, F., Noguera, C., Thromat, N., Gautier, M. & Duraud,J.P., Physical Review B **42**, 7587.

Kir61 Kirk, R. D. & Schulman, J. H., Journal of the Electrochemical Society **108**, 455.

Kol60 Koller, L. R. & Coghill, H. D., Journal of the Electrochemical Society **107**, 973.

Kor89 Koren, G., Gupta, A., Baseman, R. J., Lutwyche, M.I., & Laibowitz, R. B., Applied Physics Letters **55**, 2450.

Koy92 Koyama, T., Ohtsuka, S., Nagata, H., & Tanaka, S., Journal of Crystal Growth **117**, 156.

Lev68 Leverenz, H., An Introduction to Luminescence of Solids, Dover Publications Inc., New York, NY.

Lid97 CRC 78th Edition Handbook of Chemistry and Physics, Academic Press, Boca Raton, FL.

Mae92 Maestro, P., Huguenin, D., Seigneurin, A., & Deneuve, F., Journal of the Electrochemical Society **139**, 1470.

Map73 Maple, T., & Buchanan, R., Journal of Vacuum Science and Technology **10**, 616.

Mar88 Marshall, D., Cathodoluminescence of Geological Materials, Unwin Hyman Ltd, Boston, MA.

Mat86 Matsunawa, A., Katayama, S., Susuki, A., & Ariyasu, T., JWRI **15**, 205.

McC93 McCamy, J., Lowndes, D., Budai, J., Zuhr, R., & Zhang, X., Journal of Applied Physics **73**, 7818.

McL93 McLaughlin, M., Sakeck, H., Maquire, P., Graham, W., Molloy, J., Morrow, T., Laverty, S. & Anderson, J., Applied Physics Letters **63**, 1865.

Met94 Metev, S., Pulsed Laser Deposition of Thin Films, edited by Chrisey, D. & Hubler, G.K., John Wiley and Sons, New York, NY, chapter 9.

Mey34 Meyer-Arendt, J., Introduction to Classical and Modern Optics 2nd edition, Prentice-Hall Inc, NJ.

Nar87 Narayan, J., Biunno, N., Singh, R., Holland, O. W., & Auchiello, O., Applied Physics Letters **51**, 1845.

Neu94 Neumann-Spallart, M., Levy-Clement, C., & Grabner, G., Journal of Applied Physics D **27**, 407.

Ohr92 Ohring, M., The Materials Science of Thin Films, Academic Press, Inc., San Diego, CA.

Ort92 Ortiz, C., & Blatter, A., Thin Solid Films **218**, 209.

Ouy95 Ouyang, X., Kitai, A. H., & Siegele, R., Thin Solid Films **254**, 268.

Oza90 Ozawa, L., Cathodoluminescence: Theory and Applications, VCH Publishers, New York, NY.

Oza71 Ozawa, L., Forest, H., Jaffe, P. M., & Ban, G., Journal of the Electrochemical Society **118**, 482.

Oza68 Ozawa, L., & Jaffe, P. M., Journal of Electrochemical Society **117**, 1297.

Pea97 Peach, L. A., Laser Focus World **33**, 18.

Pin92 Pinto, R., Pai, S., P., D'Souza, C. P., Gupta, R. C., Vijayaraghavan, R., Kumar, D., & Sharon, M., Physica C **196**, 264.

Rao96 Rao, R., Solid State Comm. **99**, 439.

Rob80 Robertson, J. M., & van Tol, M. W., Applied Physics Letters **37**, 471.

Sel82 Sella, C., Martin, J., & Charreire, Y., Thin Solid Films **90**, 181.

Sie67 Siebring, B. Chemistry, Macmillan Company, New York, NY.

Sim95 Simile, M., Information Display **11**, 18.

Sin94 Singh, R. K., Journal of Non-Crystalline Solids **178**, 199.

Sin90 Singh, R. K., & Narayan, J., Physical Review B **41**, 8843.

Smi86 Smith, D., Metals Handbook 9th Edition: Vol 10 Materials Characterization, edited by Davis, J., American Society for Metals, Metals Park, Ohio.

Smi95 Smith, D. L., Thin-Film Deposition, Principles and Practices, McGraw-Hill, Inc., New York, NY.

Spi76 Spindt,C. A., Brodie, I., Humphrey, L., & Westerberg, E. R., Journal of Applied Physics **47**, 5248.

Str92 Strausser, Y.E., Encyclopedia of Materials Characterization, edited by Brundle, C.R., Evans, C.A., & Wilson, S., Manning Publications Co., chapter 5.3.

Str64 Strutt, J. W., Scientific Papers by Lord Rayleigh Volumes I & 2, Dover Publications, New York, NY.

Stu56 Studer, F.J., Journal of the SMPTE **65**, 197.

Stu55 Studer, F.J., & Cusano, D.A., Journal of the Optical Society of America **45**, 493.

Stu51 Studer, F.J., Cusano, D.A., & Young, A., H., Journal of the Optical Society of America **41**, 559.

Tan85 Tannas, L., Flat-panel displays and CRTs, van Nostrand Reinhold, New York, NY.

Tom86 Tomiki, T., Tamashiro, J., Tanahara, Y., Yamda, A., Fukutani, H., Miyahara, T., Kato, H., Shin, S., & Ishigame, M., Journal of the Physical Society of Japan **55**, 4543.

Ton92 Toney, M., Encyclopedia of Materials Characterization, edited by Brundle, C.R., Evans, C.A., & Wilson, S., Manning Publications Co., chapter 4.1.

Tro91 Tropf, W. J. & Thomas, M.E., Handbook of Optical Constants of Solids II, edited by Palik, E., Academic Press, Boston, MA.

Tro95 Tropf, W. J., Thomas, M.E., & Harris, T. J., Handbook of Optics Volume II, Academic Press, Boston, MA, chapter 33..

Uts91 Utsumi, T., IEEE Transactions on Electron Devices **38**, 2276.

Van81 VanDe Hulst, H. C., Light Scattering by Small Particles, Dover Publications, Incorporated, New York, NY.

Wes90 West, G. A & Beeson, K. W., Journal of Materials Research **5**, 1573.

Wic64 Wickersheim, K. A. & Lefever, R.A., Journal of the Electrochemical Society **111**, 47.

Wil47 William, F. E., Journal of the Optical Society of America **37**, 302.

Wu90 Wu, X., Muenchavsen, R.E., & Foltyn, S., Applied Physics Letters **56**, 1483.

Wu94 Wu, X. D., Muenchavsen, R. E., Foltyn, S., Estler, R.C., Dye, R.C., Flamme, C., Nogar, N.S., Garcia, A.R., Martin J., & Tesmer, J., Applied Physics Letters **56**, 1481.

Wyc64 Wycoff, R.W.G., Crystal Structures Volume 2, Interscience Publishers, New York, NY.

Wys78 Wyszecki, G., Handbook of Optics, edited by Drscoll, W.G., McGraw-Hill, Inc., New York, NY, chapter 9.

Yac92 Yacobi, B.G., Encyclopedia of Materials Characterization, edited by Brundle, C.R., Evans, C.A., & Wilson, S., Manning Publications Co., chapter 3.3.

BIOGRAPHICAL SKETCH

The author was born September 9, 1967, in Willimantic, Connecticut. His mother moved to South Carolina in 1969 where he graduated from Orangeburg Wilkinson High School, Orangeburg, SC, with honors in 1985. He received a Bachelor of Science degree in ceramic engineering from Clemson University in 1990 in Clemson, South Carolina, and a Master of Science in materials science and engineering from the University of Florida in 1995. He enjoys membership in several honor societies and professional organizations such as Beta Eta Sigma Honor Society, Alpha Sigma Mu Honor Society, Tiger Brotherhood Honorary Society, American Vacuum Society, Society for Information Display, American Ceramic Society, Materials Research Society, National Society of Black Engineers, Black Graduate Student Organization, and Alpha Phi Alpha Fraternity, Incorporated.

I certify that I have read this study and that in my opinion it conforms to acceptable standards of scholarly presentation and is fully adequate, in scope and quality, as a dissertation for the degree of Doctor of Philosophy.

Paul H Holloway

Paul H. Holloway, Chair
Professor of Materials Science and
Engineering

I certify that I have read this study and that in my opinion it conforms to acceptable standards of scholarly presentation and is fully adequate, in scope and quality, as a dissertation for the degree of Doctor of Philosophy.

Rajiv K. Singh
Professor of Materials Science and
Engineering

I certify that I have read this study and that in my opinion it conforms to acceptable standards of scholarly presentation and is fully adequate, in scope and quality, as a dissertation for the degree of Doctor of Philosophy.

R E Hummel

Rolf E. Hummel
Professor of Materials Science and
Engineering

I certify that I have read this study and that in my opinion it conforms to acceptable standards of scholarly presentation and is fully adequate, in scope and quality, as a dissertation for the degree of Doctor of Philosophy.

Stephen J. Pearton
Professor of Materials Science and
Engineering

I certify that I have read this study and that in my opinion it conforms to acceptable standards of scholarly presentation and is fully adequate, in scope and quality, as a dissertation for the degree of Doctor of Philosophy.

Timothy J Anderson

Timothy J. Anderson
Professor of Chemical Engineering

This dissertation was submitted to the Graduate Faculty of the College of Engineering and to the Graduate School and was accepted as partial fulfillment of the requirements for the degree of Doctor of Philosophy.

December, 1997

Winfred M. Phillips
Dean, College of Engineering

Karen A. Holbrook
Dean, Graduate School

LD
1780
1997
.J785

UNIVERSITY OF FLORIDA
3 1262 08555 0472